On the detection of nonlinear normal mode-related isolated branches of periodic solutions for high-dimensional nonlinear mechanical systems with frictionless contact interfaces

Thibaut Vadcard, Fabrice Thouverez, Alain Batailly

POLYTECHNIQUE MONTRÉAL
UNIVERSITÉ D'INGÉNIERIE

LABORATOIRE D'ANALYSE VIBRATOIRE ET ACOUSTIQUE

On the detection of nonlinear normal mode-related isolated branches of periodic solutions for high-dimensional nonlinear mechanical systems with frictionless contact interfaces

T. Vadcard[1,2], F. Thouverez[2], A. Batailly[1]

Abstract

This contribution introduces a methodology for the detection of isolated branches of periodic solutions to the nonlinear mechanical equation of motion for systems featuring frictionless contact interfaces. This methodology relies on a harmonic balance method-based solving procedure combined with the application of the Melnikov energy principle. It is able to predict the location of isolated branches of solutions in the vicinity of families of autonomous periodic solutions, namely nonlinear normal modes. The methodology is first applied on a two-degree-of-freedom phenomenological system in order to illustrate its relevance and accuracy. In particular, for this academic application, the proposed methodology yields an understanding of the discontinuous evolution of the first nonlinear resonance frequency as the forcing amplitude increases. Isolated branches of solutions featuring high amplitudes of vibration are detected far beyond nonlinear resonance frequencies obtained with a typical application of the harmonic balance method coupled with an arc-length continuation algorithm. Demonstration of the applicability of the proposed methodology to high-dimensional industrial finite element models is made with the nonlinear vibration analysis of a transsonic compressor blade, NASA rotor 37, subjected to an harmonic loading and blade-tip/casing structural contacts. The proposed methodology yields numerous isolated branches of solutions, which relevance is assessed by means of time integration simulations. In the end, the presented results underline that typical continuation algorithms may yield a significant underestimation of nonlinear resonance frequencies.

Keywords

Harmonic Balance Method,unilateral contact, nonsmooth dynamics, isolated branches, Melnikov's energy principle, blade-tip/casing interactions

1 - Département de génie mécanique, École Polytechnique de Montréal, P.O. Box 6079, Succ. Centre-Ville, Montréal, Québec, Canada H3C 3A7
2 - École Centrale de Lyon, Laboratoire de Tribologie et Dynamique des Systèmes, UMR CNRS 5513, 36 avenue Guy de Collongue, Écully, 69134, France

Détection de branches de solutions périodiques isolées liées à un mode normal non linéaire pour des systèmes mécaniques non linéaires de grande dimension avec des interfaces de contact sans frottement

T. Vadcard[1,2], F. Thouverez[2], A. Batailly[1]

Résumé

Cette contribution introduit une méthodologie permettant la détection de branches de solutions périodiques isolées de l'équation de mouvement mécanique non linéaire pour des systèmes avec des interfaces de contact sans frottement. Cette méthodologie repose sur une procédure de résolution basée sur la méthode d'équilibrage harmonique combinée à l'application du principe énergétique de Melnikov. Elle est capable de prédire l'emplacement des branches de solutions isolées à proximité des familles de solutions périodiques autonomes, à savoir les modes normaux non linéaires. La méthodologie est d'abord appliquée à un système phénoménologique à deux degrés de liberté afin d'illustrer sa pertinence et sa précision. En particulier, pour cette application académique, la méthodologie proposée permet de comprendre l'évolution discontinue de la première fréquence de résonance non linéaire lorsque l'amplitude du forçage augmente. Des branches de solutions isolées présentant de fortes amplitudes de vibration sont détectées bien au-delà des fréquences de résonance non linéaires obtenues avec une application classique de la méthode d'équilibrage harmonique couplée à un algorithme de continuation par longueur d'arc. L'applicabilité de la méthodologie proposée à des modèles industriels à éléments finis de grande dimension est demontrée en réalisant l'analyse des vibrations non linéaires d'une aube de compresseur transsonique, le rotor 37 de la NASA, soumise à une excitation harmonique et à des contacts structurels entre l'aube et le carter. La méthodologie proposée prédit l'existence de nombreuses branches de solutions isolées, dont la pertinence est évaluée au moyen de simulations d'intégration temporelle. Enfin, les résultats présentés soulignent que l'utilisation d'algorithmes de continuation classiques peuvent entraîner une sous-estimation significative des fréquences de résonance non linéaires.

Mots-clés

Méthode d'équilibrage harmonique, contact unilatéral, dynamique non régulière, branches isolées, principe énergétique de Melnikov, interactions aube/carter

1 - Département de génie mécanique, École Polytechnique de Montréal, P.O. Box 6079, Succ. Centre-Ville, Montréal, Québec, Canada H3C 3A7
2 - École Centrale de Lyon, Laboratoire de Tribologie et Dynamique des Systèmes, UMR CNRS 5513, 36 avenue Guy de Collongue, Écully, 69134, France

1 Introduction

The analysis of nonlinear dynamical systems is a very active field of research. Indeed, most industrial systems are, to a certain degree, nonlinear and may thus present a highly complex dynamics response featuring a wide variety of sophisticated vibratory behaviors [1]. The latter include bifurcations, chaotic responses, nonlinear modal interactions as well as isolated branches of solutions that may have detrimental consequences in terms of performance, lifespan or even safety of the system. In a competitive global economy, and with new regulations and norms constraining engineers to reduce the environmental footprint of several key engineering systems for energy production [2] or transportation [3] for instance, it becomes necessary to account for nonlinear behaviors in order to ensure high performances as well as low emissions. In this context, the lack of a unified theoretical framework for the analysis of nonlinear mechanical systems calls for the development of specific numerical methodologies for the design of modern industrial systems.

Developing methodologies well-suited for the prediction of sophisticated nonlinear behaviors is a multifaceted challenge. On the one hand, there has been significant advances for the prediction of specific and sophisticated nonlinear behaviors in the past years [4, 5, 6, 7], but researchers oftentimes focused on low-dimensional systems. Though such systems may exhibit an extremely rich dynamics response, their low number of degrees of freedom is not representative of that of industrial systems for which significant challenges in terms of numerical implementation may arise. On the other hand, when dealing with industrial applications, recent developments were made with an emphasis on modeling—including slender structure's large displacements [8], the estimation of friction damping rates in blade/disk assemblies [9] or inter-blade shroud contacts [10]—and the characterization of instabilities [11] or nonlinear structural interactions [12], but more fundamental aspects are oftentimes overlooked because the prediction and interpretation of complex nonlinear behaviors on high-dimensional systems is arduous.

As nonlinear mechanical applications are very diverse, each configuration usually comes with very specific challenges preventing the emergence of unified methodologies for the nonlinear analysis of mechanical systems. Developing and validating systematic numerical methodologies dedicated to the prediction of nonlinear phenomena for a class of nonlinear industrial systems is thus a step towards industry-ready strategies, allowing for increased modeling accuracy in early stages of design.

Among the aforementioned nonlinear phenomena of interest, the detection of isolated branches of solutions is crucial. Indeed, solutions belonging to isolated branches were identified to potentially be of higher amplitude and more frequentially shifted than the classical nonlinear resonances by Detroux *et al.* [13], Petrov [14] and Mangussi *et al.* [15], thus making them critical from a design viewpoint. Yet, no industrial standard strategy exists to date. As a matter of fact, the detection of isolated branches is an arduous task since no information nor on the location or on the characteristics of these solutions is known beforehand.

Isolated branches have been identified on numerous phenomenological [4, 5, 14, 15, 16, 17, 18, 19, 20, 21, 22, 23, 24] and industrial nonlinear systems [6, 25, 26, 27], but no ready-to-use strategy was yet proposed to state if isolas exist and to locate them in case they exist. Indeed, isolated branches are generally observed by researchers without having been sought for. Therefore, only few contributions explain their appearance through physical analyses. To date, some physical mechanisms have been identified, for instance Detroux *et al.* [13] and Mangussi *et al.* [13] showed that nonlinear modal interactions are likely to isolate a nonlinear resonance from the main frequency response curve, Cenedese and Haller [18] derived an energy-based principle able to locate isolated branches, some elements of response were also given by Alcorta *et al.* [23] for subharmonic isolas. Recently, methodologies were developed in order to compute isolated solutions, for instance by tracking limit-point bifurcations [4, 7, 24], by using homotopy methods [28], by using strategies relying on Groebner bases [17, 21] or with the global terrain method [6]. As a way of using a favorable framework for the development of these strategies, low-dimensional systems featuring smooth nonlinearities are generally studied. Therefore, strategies allowing to detect isolated solutions are often associated with differentiability hypotheses on the objective function and the solutions. Given these numerical strategies are also very computationally costly, it oftentimes makes them ill-suited to deal with high-dimensional industrial systems.

On the contrary, systems featuring contact nonlinearities are generally considered as one of the most adverse applications when it comes to developing new nonlinear analysis strategies. Indeed, the nonsmooth nature of nonlinear contact forces is generally associated with numerous numerical challenges. For instance, the evaluation of contact forces is a laborious task since no explicit expression exists to describe unilateral contact conditions.

Systems featuring contact interfaces are also subject to velocity discontinuities preventing the use of strategies that rely on smoothness hypotheses [4, 6, 17, 21]. The resolution of numerical contact problems is also known to be more difficult because of the stiff interactions at stake. The inherent challenges of contact interactions thus constitute a major difficulty for the development of strategies able to tackle nonlinear problems encountered on engineering applications.

For nonlinear dynamical contact problems, several solution paradigms coexist. Direct time-domain approaches relying on time integration are usually favored when it comes to producing reference simulations. Time domain strategies are generally associated with higher computing costs because almost no assumptions are made on the solutions of the problem [29, 30, 31, 32]. Time integration algorithms are now widely used for the characterization of the highly nonlinear rubbing interactions in turbomachinery [33, 34, 35, 36]. More recently, the harmonic balance method (HBM), based on the frequency-domain paradigm, became popular for the research of periodic solutions for contact problems. It was applied to phenomenological models [5, 37] and even industrial configurations [14, 25, 27, 38]. The periodicity assumption of the HBM advantageously yields a drop in computing times. Numerical methods relying on the frequency domain also allow access to qualitative aspects of nonlinear systems, such as the stability of periodic orbits [39, 40, 41] or the continuity of branches of solutions [5, 25].

Very recently, Cenedese and Haller [18] proposed an analytical criterion allowing to predict the existence of solutions in a forced/damped configuration by performing an energy analysis on conservative solutions of nonlinear normal modes (NNM) of a system. This concept is based on the analysis of the so-called Melnikov function. Studying the zeros of this function allows to state on the persistence of periodic orbits for a conservative family when they are subjected to a weak perturbation. This method has been used both for the study of regular [42, 43, 44] and non regular [45, 46, 47] nonlinear systems. In all cases, these studies were conducted on small systems. In fact, the energy principle formulated by Cenedese and Haller [18] was already used as a heuristic in the literature [48, 49, 50, 51] also known as the energy balance method. Among the most recent contributions, Melnikov's energy principle was applied on a low-dimensional system featuring a smooth nonlinearity [18] and on a parametric oscillator featuring dry friction [19]. In both cases the methodology allowed to locate isolated branches of solutions for phenomenological models. In addition, the Melnikov analysis is easily embedded in the workflow of analysis of nonlinear systems because it relies on inexpensive calculations based on NNM. For that reason, Melnikov analysis appears to be a very promising methodological tool applicable to all types of systems and nonlinearities, providing new insights on the physical mechanisms responsible of the existence of isolated solutions with an emphasis on isolated branches that are associated to a NNM.

This article aims to demonstrate both the accuracy and the applicability of a numerical isola detection procedure on a high-dimensional nonlinear mechanical application featuring contact interfaces. It is focused on isolated branches of solutions associated to a NNM and do not account for isolated branches of solutions that seem to be unrelated to nonlinear normal modes [17]. This last point is in fact an active field of research since an exhaustive listing of nonlinear modes (with all their bifurcated branches) of a system can even be impossible in some configurations where a very large (if not infinite) number of nonlinear modes may exist [28]. Moreover, finding all branches associated to a nonlinear mode on nonsmooth applications can be arduous since most of the strategies require the computation of second-order derivatives to located new branches [52]. Finally, finding an isolated branch without locating a nonlinear normal mode in its vicinity does not necessarily imply that it is not related to a nonlinear mode but rather that one mode may not have been detected.

In section 2, the whole numerical framework is presented, including: key HBM equations, the evaluation of nonlinear contact forces, the computation of NNM, the arc-length continuation procedure and the application of the energy principle. An amplitude-dependent nonlinear behavior is observed on a low-dimensional phenomenological model in section 3 and explained through the application of the presented isola detection procedure. Finally, an application of the methodology on the NASA rotor 37 blade with a damped NNM is given in section 4. It demonstrates the applicability of the isola detection procedure on a high-dimensional industrial blade model undergoing rubbing interactions.

2 Numerical framework

The space and time normalized equation of motion for a n-dof (degrees of freedom) system reads

$$\frac{\alpha}{\beta^2}\mathbf{M}\ddot{\mathbf{x}}(t) + \frac{\alpha}{\beta}\mathbf{C}\dot{\mathbf{x}}(t) + \alpha\mathbf{K}\mathbf{x}(t) + \mathbf{f}_{\text{nl}}(\mathbf{x}(t), \dot{\mathbf{x}}(t)) = \mathbf{f}_{\text{ex}}(\omega, t) \tag{1}$$

where $\mathbf{x}$ is the unknown displacement field, $\mathbf{M}$, $\mathbf{C}$ and $\mathbf{K}$ are the constitutive mass, damping and stiffness matrices of the system. ω is the fundamental pulsation of the excitation. α and β are respectively the space normalization and time normalization coefficients chosen so that $\alpha \|\mathbf{x}\| \simeq 1$ and $\omega/\beta \simeq 1$ for the sake of numerical conditioning. $\mathbf{f}_{\text{nl}}(\mathbf{x}(t), \dot{\mathbf{x}}(t))$ are the nonlinear forces depending on the displacement and velocity fields. Finally $\mathbf{f}_{\text{ex}}(\omega, t)$ are the harmonic excitation forces also referred to as external forcing.

For this work, the nonlinear term $\mathbf{f}_{\text{nl}}(\mathbf{x}(t), \dot{\mathbf{x}}(t))$ of Eq. (1) is used to model contact interactions. The computation of the contact forces is based on the respect of the unilateral contact constraints [53] (or Hertz-Signorini-Moreau conditions). The excitation forces are chosen to be harmonic of fundamental period $T = \frac{2\pi}{\omega}$. The Harmonic Balance Method [54] (HBM) makes the hypothesis that this periodicity also translates to the solution displacement field, this methodology is detailed in section 2.1.

2.1 Harmonic balance method

In the case of a mechanical system withstanding monoharmonic excitation forces of the form $\mathbf{f}_{\text{ex}}(t) = \mathbf{a}_1^{\text{ex}} \cos(\omega t) + \mathbf{b}_1^{\text{ex}} \sin(\omega t)$, the HBM [54] relies on the assumption that the displacement field $\mathbf{x}(t)$ can be written as a truncated Fourier series with N_{h} harmonics, such as

$$\mathbf{x}(t) \simeq \frac{1}{2}\mathbf{a}_0 + \sum_{k=1}^{N_{\text{h}}} \left(\mathbf{a}_k \cos(k\omega t) + \mathbf{b}_k \sin(k\omega t)\right) \tag{2}$$

where $\mathbf{a}_k$ and $\mathbf{b}_k$ are the real Fourier coefficients, the new unknowns of the problem. In a similar way as $\mathbf{x}(t)$, it is possible to express $\mathbf{f}_{\text{nl}}(t)$ as truncated Fourier series with $\mathbf{a}_k^{\text{nl}}$ and $\mathbf{b}_k^{\text{nl}}$ being the real Fourier coefficients of the nonlinear forces. Each $\mathbf{a}_k^\bullet$ and $\mathbf{b}_k^\bullet$ for $\bullet = \{-, \text{nl}, \text{ex}\}$ is a vector of size n of the form

$$\begin{cases} \mathbf{a}_k^\bullet = [a_k^{\bullet,1}, a_k^{\bullet,2}, \dots, a_k^{\bullet,n}]^\top \text{ for } k \in [\![0, N_{\text{h}}]\!] & \text{(3a)} \\ \mathbf{b}_k^\bullet = [b_k^{\bullet,1}, b_k^{\bullet,2}, \dots, b_k^{\bullet,n}\ ]^\top \text{ for } k \in [\![1, N_{\text{h}}]\!]. & \text{(3b)} \end{cases}$$

In the end, these coefficients are concatenated in so-called multiharmonic vectors of size $n(2N_{\text{h}}+1)$ that read

$$\begin{cases} \widetilde{\mathbf{x}} = [\mathbf{a}_0^\top\ \mathbf{a}_1^\top\ \mathbf{b}_1^\top \dots\ \mathbf{a}_{N_{\text{h}}}^\top\ \mathbf{b}_{N_{\text{h}}}^\top]^\top & \text{(4a)} \\ \widetilde{\mathbf{f}}_{\text{nl}} = [(\mathbf{a}_0^{\text{nl}})^\top\ (\mathbf{a}_1^{\text{nl}})^\top\ (\mathbf{b}_1^{\text{nl}})^\top \dots\ (\mathbf{a}_{N_{\text{h}}}^{\text{nl}})^\top\ (\mathbf{b}_{N_{\text{h}}}^{\text{nl}})^\top]^\top & \text{(4b)} \\ \widetilde{\mathbf{f}}_{\text{ex}} = [\mathbf{0}\ (\mathbf{a}_1^{\text{ex}})^\top\ (\mathbf{b}_1^{\text{ex}})^\top\ \mathbf{0}\ \dots\ \mathbf{0}\ \mathbf{0}]^\top. & \text{(4c)} \end{cases}$$

This formalism is then used to perform a Fourier-Galerkin projection on the nonlinear differential equation of motion, based on the Fourier basis $\mathbf{B}_{N_{\text{h}}}$ composed of N_{h} harmonics. It yields a nonlinear algebraic system of $n(2N_{\text{h}}+1)$ equations concatenated in the vectorial equation

$$\mathcal{H}(\widetilde{\mathbf{x}}, \omega) = \mathbf{Z}(\omega)\widetilde{\mathbf{x}} + \widetilde{\mathbf{f}}_{\text{nl}}(\widetilde{\mathbf{x}}) - \widetilde{\mathbf{f}}_{\text{ex}} = \mathbf{0} \tag{5}$$

where the dynamic stiffness matrix $\mathbf{Z}(\omega)$ is block-diagonal. The definitions of its $N_{\text{h}}+1$ blocks $\mathbf{Z}_k$ are

$$\mathbf{Z}_0 = \alpha\mathbf{K} \quad \text{and} \quad \mathbf{Z}_k(\omega) = \alpha \begin{bmatrix} \mathbf{K} - \left(\frac{k\omega}{\beta}\right)^2 \mathbf{M} & \frac{k\omega}{\beta}\mathbf{C} \\ -\frac{k\omega}{\beta}\mathbf{C} & \mathbf{K} - \left(\frac{k\omega}{\beta}\right)^2 \mathbf{M} \end{bmatrix} \quad \forall k \in [\![1, N_{\text{h}}]\!]. \tag{6}$$

For the sake of computational efficiency, two steps of exact condensation are employed in order to reduce the size of Eq. (5). Both condensation strategies are detailed in A and their application yields the following condensed equation of motion

$$\mathcal{H}_{\mathrm{r}}(\widetilde{\mathbf{x}}_{\mathrm{r}},\omega)=\mathbf{Z}_{\mathrm{r}}(\omega)\widetilde{\mathbf{x}}_{\mathrm{r}}+\widetilde{\mathbf{f}}_{\mathrm{nl,r}}-\widetilde{\mathbf{f}}_{\mathrm{ex,r}}=\mathbf{0}. \tag{7}$$

where the relative displacement (homogeneous to a gap) $\widetilde{\mathbf{x}}_{\mathrm{r}}$ is the new unknown.

2.2 Dynamic Lagrangian frequency/time

Nonlinear forces are *a priori* unknown and their evaluation in the frequency domain may be challenging. As a way of circumventing this difficulty, the nonlinear harmonic equation of motion should be solved iteratively with a Newton-Raphson algorithm computing an estimate of the contact forces at each iteration relying on a contact model. For vibro-impact problems, the choice of contact modeling is critical for the sake of representativeness. For frequency-domain strategies such as the HBM, the evaluation of contact forces is exclusively made through an alternating frequency/time (AFT) strategy [55], relying on the evaluation of nonlinear forces in the time domain before projecting them back into the frequency domain. Several so-called contact laws coexist for the computation of nonlinear forces based on the knowledge of a displacement field estimate. Penalty laws are commonly used because they allow for a direct computation of nonlinear forces based on an analytical expression. Among this family, one may cite the classical nonsmooth penalty law [23, 56, 57, 58, 59, 60, 61, 62] or the newly proposed regularized-Lanczos penalty law [25, 38, 39]. More recently, the dynamical Lagrangian frequency/time (DLFT) methodology [63]—developed for friction damping applications [6, 27, 64]—was proven to be suitable for the resolution of stiff vibro-impact problems [25, 37]. The latter is considered in this work for the sake of modeling accuracy. The current section contains the main aspects of the DLFT-HBM methodology, but more details about this strategy were given in a study dealing with a low-dimensional vibro-impact phenomenological model [37].

The DLFT-HBM is an alternate version of the AFT scheme where the computation of nonlinear forces requires a prediction step followed by a correction. The strategy is built such that nonlinear forces are evaluated thanks to the knowledge of $\widetilde{\mathbf{x}}_{\mathrm{r}}$ at each iteration of the optimization solver. The prediction step at the k-th iteration, denoted by k superscripts, is

$$\widetilde{\boldsymbol{\lambda}}_{\mathbf{x}}^{k}=\widetilde{\mathbf{f}}_{\mathrm{ex,r}}-\mathbf{Z}_{\mathrm{r}}\widetilde{\mathbf{x}}_{\mathrm{r}}^{k}-\varepsilon\widetilde{\mathbf{g}}_{\mathbf{x}}^{k} \tag{8}$$

where $\widetilde{\boldsymbol{\lambda}}_{\mathbf{x}}^{k}$ are the predicted contact forces at iteration k. The respect of the complementarity condition between the gap function $g(t)$ and the contact force $\lambda(t)$ is ensured by the introduction of a penalization term $\varepsilon\widetilde{\mathbf{g}}_{\mathbf{x}}$ in the prediction step, where ε is a weighting parameter and $\widetilde{\mathbf{g}}_{\mathbf{x}}$ is the gap function expressed in the frequency domain: $\widetilde{\mathbf{g}}_{\mathbf{x}}=\widetilde{\mathbf{x}}_{\mathrm{r}}+\widetilde{\mathbf{g}}_{0}$ with $\widetilde{\mathbf{g}}_{0}$ being the multiharmonic vector representing the initial gap between both structures.

It is not possible to perform the correction step in the frequency domain, thus it is necessary to perform an inverse discrete Fourier transform (IDFT) of the predicted contact forces on N_{t} evenly spaced time instants. This is done by multiplying the multiharmonic vector $\widetilde{\boldsymbol{\lambda}}_{\mathbf{x}}^{k}$ by the IDFT matrix $\overline{\mathcal{F}}$ expressed with the Fourier Basis $\mathbf{B}_{N_{\mathrm{h}}}$. The Discrete Fourier Transform (DFT) is expressed as the Moore-Penrose pseudo-inverse matrix of $\overline{\mathcal{F}}$, written in the form $\mathcal{F}=\overline{\mathcal{F}}^{\top}\left(\overline{\mathcal{F}}.\overline{\mathcal{F}}^{\top}\right)^{-1}$.

One can note that the pseudo-inverse of $\overline{\mathcal{F}}$ is equivalent to a standard forward DFT matrix built by an analytical expression, while always ensuring that $\mathcal{F}\overline{\mathcal{F}}=\mathbf{I}_{N_{\mathrm{t}}}$. Once the contact forces are known in the time domain, the correction step takes place at each time t_i. The corrected contact forces read $\lambda^{k}(t_i)=\lambda_{\mathbf{x}}^{k}(t_i)+\lambda_{\mathbf{y}}^{k}(t_i)$. For normal contact forces, there are two cases distinguished by the sign of the prediction $\lambda_{\mathbf{x}}^{k}$ at time t_i:

- **separation** ($\lambda_{\mathbf{x}}^{k}(t_i)<0$): the contact force should be zero, implying that $\lambda^{k}(t_i)=0$ and $\lambda_{\mathbf{y}}^{k}(t_i)=-\lambda_{\mathbf{x}}^{k}(t_i)$,
- **contact** ($\lambda_{\mathbf{x}}^{k}(t_i)>0$): the contact force should be equal to the prediction, so $\lambda^{k}(t_i)=\lambda_{\mathbf{x}}^{k}(t_i)$ and $\lambda_{\mathbf{y}}^{k}(t_i)=0$.

Once the correction is made on all time instants, it ensures that the contact forces stay valid (positive sign convention) throughout the whole period. Following this step, the multiharmonic vector of contact forces is computed through a DFT allowing to evaluate the residual of the objective function $\mathcal{H}_{\mathrm{r}}(\widetilde{\mathbf{x}}_{\mathrm{r}},\omega)$. This procedure is summed up in Fig. 1. Further details on the computation of the jacobian matrix of the system can be found in the literature [37].

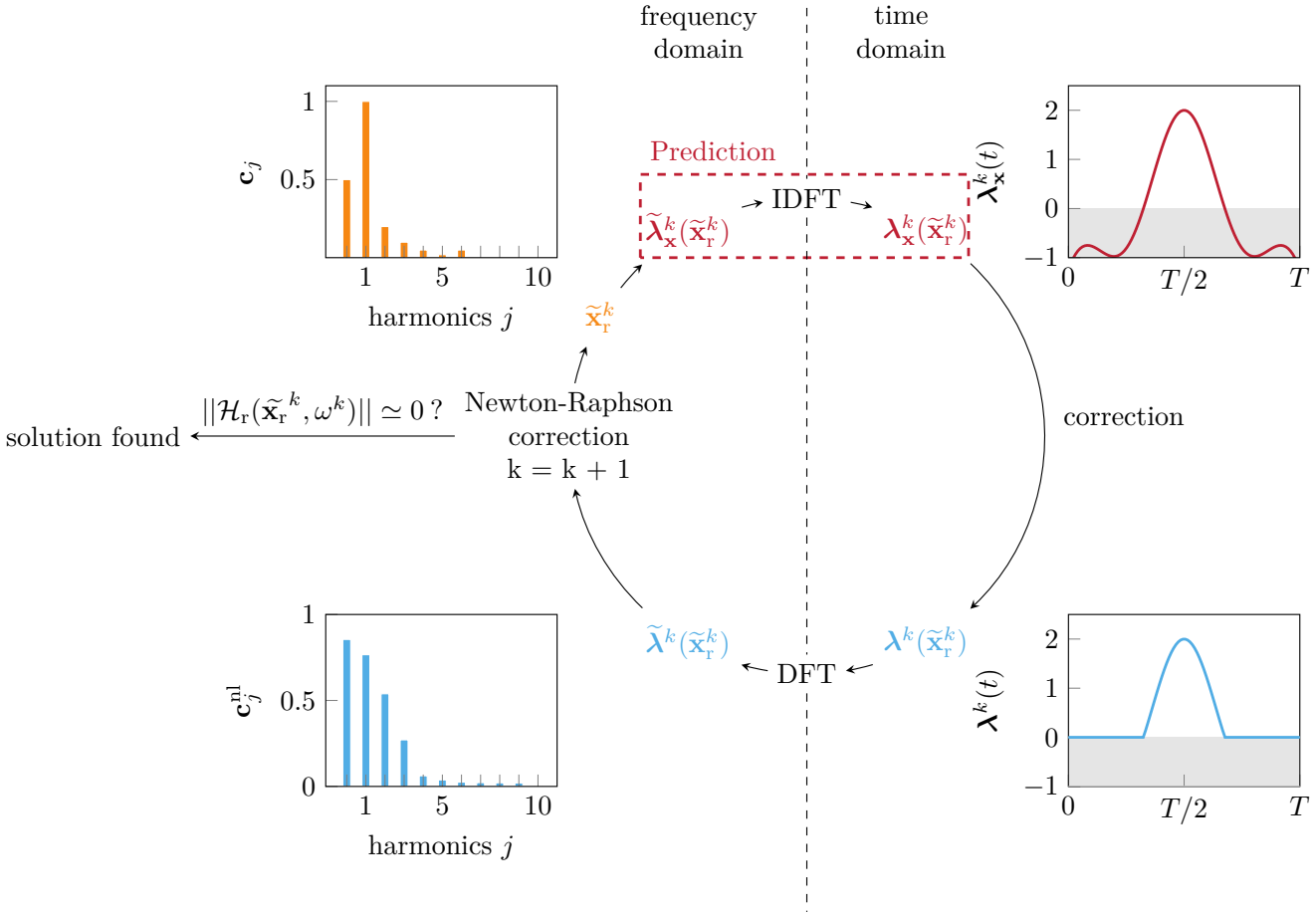

Figure 1. DLFT-HBM procedure.

2.3 Conservative nonlinear normal modes

Linear modal analysis is a powerful tool that allows to define the eigenproperties of a mechanical system. A first extension from linear to nonlinear modal analysis was introduced by Rosenberg [65] and a second one later on by Shaw and Pierre [66], both defining the notion of nonlinear normal mode (NNM). Following these theoretical definitions, several numerical methods are able to compute the family of solutions composing a NNM, for instance the shooting method [67, 68, 69] and the HBM [70, 71]. These strategies have to be coupled with a continuation strategy, for instance the arc-length continuation [72], in order to account for the energy-level dependence of eigenfrequencies and mode shapes of NNM. Extensions of NMM to damped and nonconservative systems were proposed by Laxalde and Thouverez [70] and Krack [73], the latter methodologies were benchmarked by Sun *et al.* [74]. This section describes the methodology used to compute the conservative NNM of a system with the HBM.

The computation of the conservative NNM of a mechanical system consists in solving the normalized autonomous nonlinear equation of motion

$$\frac{\alpha}{\beta^2}\mathbf{M}\ddot{\mathbf{x}}(t) + \alpha\mathbf{K}\mathbf{x}(t) + \mathbf{f}_{\text{nl}}(\mathbf{x}(t), \dot{\mathbf{x}}(t)) = \mathbf{0}. \tag{9}$$

Equation (9) is a special case of Eq. (1) with $\mathbf{C} = \mathbf{0}$ and $\mathbf{f}_{\text{ex}}(\omega, t) = \mathbf{0}$, allowing both for the use of the HBM formulation (section 2.1) and for the use of the DLFT strategy (section 2.2) to evaluate nonlinear forces. The

condensed autonomous HBM nonlinear equation reads

$$\mathbf{Z}_{\mathrm{r}}(\omega)\widetilde{\mathbf{x}}_{\mathrm{r}} + \widetilde{\mathbf{f}}_{\mathrm{nl,r}}(\widetilde{\mathbf{x}}_{\mathrm{r}}) = \mathbf{0}. \tag{10}$$

At very low energy levels, *i.e.* when the nonlinearity is not—or weakly—activated, the linear mode is tangent to the NNM. This property is useful since it allows to provide points of initialization for the computation of the mode. A NNM is computed by means of a continuation strategy going from the low amplitudes to the high amplitudes. The arc-length continuation strategy is retained for this work and it is presented in section 2.4.1. This method requires two points to be able to compute further points [72]. In order to compute the NNM associated with the first linear mode defined by the modal properties $(\omega_{\Phi_1}, \Phi_1)$, two points $(\widetilde{\mathbf{x}}_1, \omega_1)$ and $(\widetilde{\mathbf{x}}_2, \omega_2)$ are chosen on the linear mode such that

$$\widetilde{\mathbf{x}}_1 = \epsilon_1 \mathcal{F}\Phi_1 \left\{\cos(\omega_1 t_i)\right\}_{i=1\dots N_{\mathrm{t}}}, \ \widetilde{\mathbf{x}}_2 = \epsilon_2 \mathcal{F}\Phi_1 \left\{\cos(\omega_2 t_i)\right\}_{i=1\dots N_{\mathrm{t}}} \text{ and } \omega_1 = \omega_2 = \omega_{\Phi_1} \tag{11}$$

where $0 < \epsilon_1 < \epsilon_2$ are small scalar values chosen so that the contact nonlinearity is not activated.

When the nonlinear normal mode can not be directly initialized on a linear response (pre-loaded contacts or negative initial gaps for instance), initialization points should be found by firstly performing a static initialization of the system. This static initialization allows to provide the displacement induced by preloading effects on harmonic 0. Once the static initialization is made, the state of contact shall be examined to produce a linearized version of the system if contact is activated. Indeed, if there is a static contact between the system and the obstacle, the underlying linear mode used for initialization should be computed by clamping contact nodes that are in contact.

NNM are usually of great interest since they accurately describe the frequency dependence of nonlinear resonances. In particular, NNM are used to predict asymptotic nonlinear resonance frequencies. These frequencies are generally too computationally expensive to be uncovered through classical forced-response calculations.

2.4 Continuation procedure

2.4.1 Arc-length continuation

The arc-length continuation procedure [72] consists in augmenting the nonlinear harmonic equation of motion with a local parameterization of the curve $\mathcal{P}_\omega$ and considering the excitation pulsation ω as a supplementary unknown. The parameterization equation (12) for the $(i+1)$-th point reads

$$\mathcal{P}_\omega(\widetilde{\mathbf{x}}, \omega) = \|\widetilde{\mathbf{x}} - \widetilde{\mathbf{x}}_i\|_2^2 + (\omega - \omega_i)^2 - \mathrm{d}s^2. \tag{12}$$

This parameterization ensures that two consecutive solutions are found at the intersection of the solution space and an hypersphere of radius ds centered around the last solution found $(\widetilde{\mathbf{x}}_i, \omega_i)$. The arc-length continuation procedure is summed up in Fig. 2a.

2.4.2 Detection of isolas

Since isolated branches are encountered in the field of nonlinear dynamics, it is necessary to define a procedure to detect when a branch of solutions is isolated. In order to do so, a criterion is used to decide if the continuation procedure is looping. As a way of defining this criterion, one should save the first point of the continuation $(\widetilde{\mathbf{x}}_1, \omega_1)$ as a reference. If, further in the continuation, two successive points—say the i-th and $(i+1)$-th—go through the pulsation of the first point ω_1, then a test is performed in order to state if the continuation has looped. This is done by interpolating between both solutions $(\widetilde{\mathbf{x}}_i, \omega_i)$ and $(\widetilde{\mathbf{x}}_{i+1}, \omega_{i+1})$ at the pulsation ω_1, such that the interpolated multiharmonic vector $\widetilde{\mathbf{x}}_{\mathrm{int}}$ is

$$\widetilde{\mathbf{x}}_{\mathrm{int}} = \widetilde{\mathbf{x}}_i + \frac{\omega_1 - \omega_i}{\omega_{i+1} - \omega_i}(\widetilde{\mathbf{x}}_{i+1} - \widetilde{\mathbf{x}}_i). \tag{13}$$

If the relative distance between the interpolated multiharmonic vector $\widetilde{\mathbf{x}}_{\text{int}}$ and $\widetilde{\mathbf{x}}_1$, computed by means of the formula

$$d_{\text{int}} = \frac{\|\widetilde{\mathbf{x}}_{\text{int}} - \widetilde{\mathbf{x}}_1\|_2}{\|\widetilde{\mathbf{x}}_{\text{int}}\|_2}, \tag{14}$$

is smaller than a user-defined tolerance, an isolated branch is detected because the curve has passed through the same point twice in the $n(2N_{\text{h}}+1)$-dimensional resolution space. The interpolation procedure is represented in Fig. 2b.

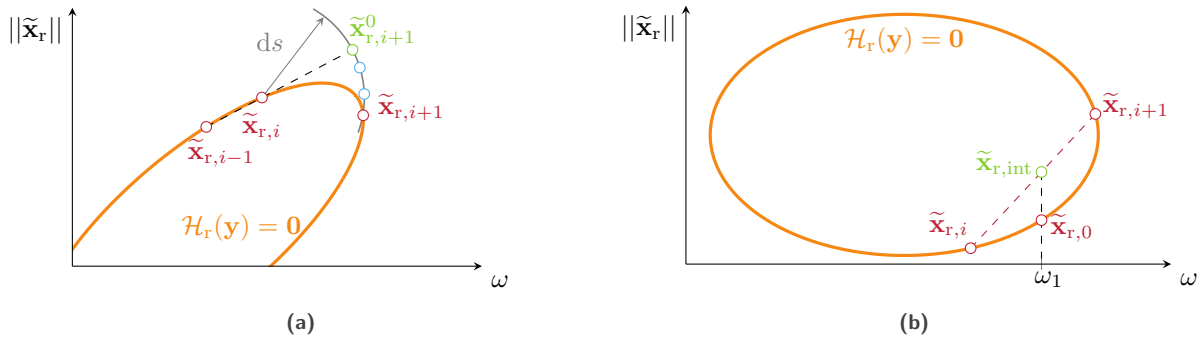

Figure 2. Continuation strategy, solutions subspace (—), direction of research (—), solutions (○), prediction (○), correction iterations (○).

2.5 Energy based principle: Melnikov analysis

The energy principle proposed by Cenedese and Haller [18] is based on a perturbation analysis using the non conservative perturbation $\mathbf{q}(\mathbf{x}, \dot{\mathbf{x}}, \tau)$ including both forcing and dissipative terms. For an harmonic excitation of amplitude A with the normalized shape $\mathbf{f}_{\text{ex}}$ and viscous damping, this perturbation reads

$$\mathbf{q}(\mathbf{x}, \dot{\mathbf{x}}, \tau) = A\mathbf{f}_{\text{ex}} \cos(\omega\tau) - \mathbf{C}\dot{\mathbf{x}}. \tag{15}$$

In order to derive the relations for the detection of solutions bifurcating from undamped free solutions, one must firstly examine the energy balance of periodic solutions over one period. For any T-periodic solution $\mathbf{x}_{\text{p}}(t)$, the work produced both by conservative and non-conservative terms is zero over one period. Since this property is implicitly verified for the conservative part, one only has to verify that the work $\mathcal{W}$ of the perturbation $\mathbf{q}$ should be zero over one period, yielding

$$\mathcal{W} = \int_0^T \langle \dot{\mathbf{x}}_{\text{p}}(\tau), \mathbf{q}(\mathbf{x}_{\text{p}}(\tau), \dot{\mathbf{x}}_{\text{p}}(\tau), \tau) \rangle \mathrm{d}t = 0. \tag{16}$$

Cenedese and Haller [18] showed that if $\mathbf{q}$ is a small perturbation compared to the conservative part of the equation of motion, then the first-order term of the Taylor expansion of Eq. (16) centered around the conservative part of the solution $\mathbf{x}_{\text{c}}(t)$ is in fact the Melnikov function $\mathcal{M}$ that reads

$$\mathcal{M}(t) = \int_0^T \langle \dot{\mathbf{x}}_{\text{c}}(t+\tau), \mathbf{q}(\mathbf{x}_{\text{c}}(t+\tau), \dot{\mathbf{x}}_{\text{c}}(t+\tau), t+\tau) \rangle \mathrm{d}\tau. \tag{17}$$

Equation (17) refers to the work of the damping and forcing terms in $\mathbf{q}$ over a period of the free conservative part of the solution $\mathbf{x}_{\text{c}}$. The perturbation $\mathbf{q}$, in the form given in Eq. (15), can be substituted into Eq. (17) in order to simplify the Melnikov function and it yields

$$\mathcal{M}^{1:1}(t) = w^{1:1}(A, \mathbf{f}_{\text{ex}}, t) - \mathcal{R}(\mathbf{C}). \tag{18}$$

The $\bullet^{1:1}$ superscript refers to the fact that—in the presented case—both the period of the excitation forces and the period of the conservative part of the solution are equal to T. The forcing term $w^{1:1}(A, \mathbf{f}_{\text{ex}}, t)$ reads

$$w^{1:1}(A, \mathbf{f}_{\text{ex}}, t) = A \int_0^T \langle \dot{\mathbf{x}}_c(t+\tau), \mathbf{f}_{\text{ex}} \rangle \cos(\omega\tau) \mathrm{d}\tau \tag{19}$$

and the dissipative term, also called the resistance term, is

$$\mathcal{R}(\mathbf{C}) = \int_0^T \langle \dot{\mathbf{x}}_c(t+\tau), \mathbf{C}\dot{\mathbf{x}}_c(t+\tau) \rangle \mathrm{d}\tau. \tag{20}$$

In the HBM framework, the displacement field $\mathbf{x}_c(t)$ can be written as a truncated Fourier series, such that

$$\mathbf{x}_c(t) = \frac{1}{2}\mathbf{a}_0^c + \sum_{k=1}^{N_{\text{h}}} \left(\mathbf{a}_k^c \cos(k\omega t) + \mathbf{b}_k^c \sin(k\omega t) \right). \tag{21}$$

By inserting Eq. (21) into Eq. (19), the expression of the work term $w^{1:1}$ is simplified such as

$$w^{1:1}(A, \mathbf{f}_{\text{ex}}, t) = W^{1:1}(A, \mathbf{f}_{\text{ex}}) \cos\left(\omega t - \alpha_{1,\text{ex}}\right) \tag{22}$$

with $W^{1:1}(A, \mathbf{f}_{\text{ex}}) = A\pi\sqrt{\langle \mathbf{a}_1^c, \mathbf{f}_{\text{ex}} \rangle^2 + \langle \mathbf{b}_1^c, \mathbf{f}_{\text{ex}} \rangle^2}$ and $\alpha_{1,\text{ex}} = \arctan\left(\dfrac{\langle \mathbf{a}_1^c, \mathbf{f}_{\text{ex}} \rangle}{\langle \mathbf{b}_1^c, \mathbf{f}_{\text{ex}} \rangle} \right)$.

Both the resistance and the forcing terms are based on the conservative solutions of the system, it makes those terms virtual since the work of excitation forces and the dissipated energy are not appearing in the actual energy balance of the conservative solutions. According to Cenedese and Haller [18], the existence of solutions in the forced/damped configuration (*i.e.* for the perturbation defined in Eq. (15)) can be stated depending on the quantities $\left|W^{1:1}(A, \mathbf{f}_{\text{ex}})\right|$ and $|\mathcal{R}(\mathbf{C})|$ computed for a single conservative solution $\mathbf{x}_{\text{c}}(t)$:

1. if $\left|W^{1:1}(A, \mathbf{f}_{\text{ex}})\right| < |\mathcal{R}(\mathbf{C})|$, no periodic solution persists,
2. if $\left|W^{1:1}(A, \mathbf{f}_{\text{ex}})\right| = |\mathcal{R}(\mathbf{C})|$, a single periodic solution persists,
3. if $\left|W^{1:1}(A, \mathbf{f}_{\text{ex}})\right| > |\mathcal{R}(\mathbf{C})|$, two periodic solutions persist.

These three statements are made thanks to the energy balance of the perturbation $\mathbf{q}$ on the conservative solution $\mathbf{x}_{\text{c}}(t)$. If the injected energy exceeds the dissipated energy, then two periodic solutions arise. If both energies are equal, then a single periodic solution arises. Finally, if the dissipated energy exceeds the injected energy then no solution exists.

This post-processing strategy is particularly well-suited to NNM computed through HBM because the solutions composing a conservative NNM can be used to perform the presented perturbation analysis. For a given perturbation (forcing and damping), this energy balance should be computed for each point of the NNM in order to predict the areas where periodic solutions to the forced/damped problem exist in the vicinity of solutions from the NNM.

In the context of this article, a question of applicability for nonsmooth problems arises since the Melnikov's analyses rely on a smoothness hypothesis. However, since the quantities of the energy principle $W^{1:1}$ and $\mathcal{R}$ do not involve any derivatives that may be discontinuous or undefined (nonlinear forces), it is expected that no error is made when applying the energy principle. Actually, in a HBM framework, displacement and velocity fields are smooth because of the representation in the form of Fourier series. For conservative nonlinearities, all energies are then continuous and smooth as well, justifying that no problem should be encountered.

2.6 Isola detection procedure

The isola detection procedure used in this work consists in the successive use of the presented elementary methodologies. It is articulated onto four major steps, also schematized in Fig. 3:

1. the computation of a nonlinear frequency response curve (NFRC) in a forced-response configuration through an arc-length continuation using DLFT-HBM, see Fig. 3a,
2. a nonlinear modal analysis, revealing the different NNM involved in the system's dynamics response, see Fig. 3b,

3. resulting NNM are analyzed through the scope of a Melnikov analysis allowing to state whether autonomous solutions persist or not in the forced/damped configuration of step 1, see Fig. 3c,
4. new continuations are started on the portions where Melnikov predicted isolated branches, continuations are initialized on autonomous solutions belonging to the NNM in these portions, see Fig. 3d.

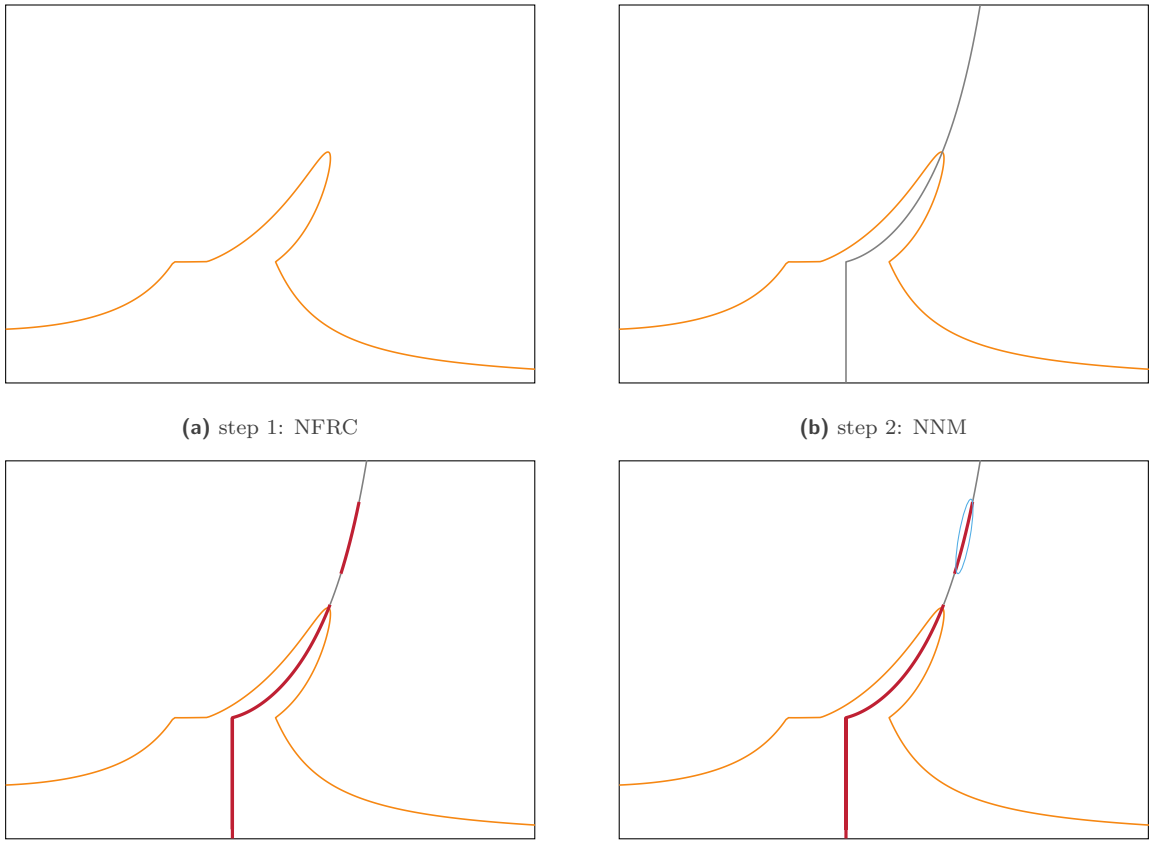

(a) step 1: NFRC **(b)** step 2: NNM

(c) step 3: Melnikov analysis **(d)** step 4: continuation

Figure 3. Different steps of the overall numerical strategy, NFRC (—), NNM (—), autonomous solutions where Melnikov criterion predicts persistence (—), isolated branch (—).

It is worth noting that the Melnikov analysis detects solutions persisting from autonomous solutions regardless of the connectivity of the different branches as well as the stability of the solutions of which they are composed. This is why the main NFRC's nonlinear resonance should also be accurately predicted. This property technically allows to skip the first step—consisting of the computation of a NFRC—if the only goal is to detect isolated branches or the tracking of the nonlinear resonance, however this step is kept in this paper for the sake of result cross-checking.

3 Numerical application: low-dimensional system subject to a single contact constraint

In this section, the isola detection procedure presented in section 2.6 is used in order to analyze the dynamics of a nonlinear low-dimensional system subject to a single contact constraint in terms of forced-response. This type of systems, also called a piecewise linear oscillator, is oftentimes studied in the literature [75, 76, 77, 78, 79, 80] in order to understand underlying contact-induced phenomena.

3.1 Phenomenological model

The system used in this article is a chain of 2 masses subject to a contact constraint. It is represented in Fig. 4. The

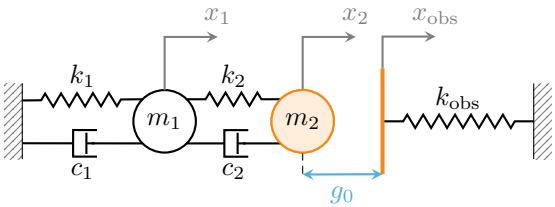

Figure 4. Phenomenological model of a 2-dof impactor.

parameters of this model are given in table 1.

i	m_i	ξ_i	k_i
1	0.5 kg	0.01	100 N·m^{-1}
2	1 kg	0.01	300 N·m^{-1}

Table 1. Values of the parameters of the system.

The constitutive matrices of the 2-dof oscillator are

$$\mathbf{M} = \begin{bmatrix} m_1 & 0 \\ 0 & m_2 \end{bmatrix} \quad \text{and} \quad \mathbf{K} = \begin{bmatrix} k_1 + k_2 & -k_2 \\ -k_2 & k_2 \end{bmatrix}. \tag{23}$$

Modal damping is applied so that the damping matrix $\mathbf{C}$ is computed such as

$$\mathbf{C} = \mathbf{M}\mathbf{\Phi}\text{diag}(2\xi_i\omega_i)\mathbf{\Phi}^\top\mathbf{M} \tag{24}$$

where ξ_i are the damping ratios, ω_i the eigenfrequencies and $\mathbf{\Phi}$ the modal shapes. The structure is forced along its first linear mode $\mathbf{\Phi}_1$ on the first harmonic such that

$$\mathbf{f}_{\text{ex}}(t) = A\mathbf{M}\mathbf{\Phi}_1\cos(\omega t). \tag{25}$$

The two modes $\mathbf{\Phi}_1$ and $\mathbf{\Phi}_2$ of the structure are $\mathbf{M}$-normalized and their numerical values are

$$\mathbf{\Phi}_1 = \begin{bmatrix} -0.702 \\ -0.868 \end{bmatrix} \text{ and } \mathbf{\Phi}_2 = \begin{bmatrix} -1.228 \\ 0.496 \end{bmatrix}. \tag{26}$$

The associated eigenfrequencies are respectively $\omega_1 = 7.58\,\text{rad·s}^{-1}$ and $\omega_2 = 32.28\,\text{rad·s}^{-1}$. For the whole study, the obstacle is considered as a massless stiffness $k_{\text{obs}} = 1 \cdot 10^4\,\text{N·m}^{-1}$. The constitutive matrices of the obstacle are $\mathbf{M}_{\text{obs}} = [0]$, $\mathbf{C}_{\text{obs}} = [0]$ and $\mathbf{K}_{\text{obs}} = [k_{\text{obs}}]$. These matrices are used to perform the relative displacement condensation where x_2 and x_{obs} form a node-to-node contact pair. The gap between the mass m_2 and the obstacle is $g_0 = 0.4\,\text{m}$ at rest. The DLFT-HBM computations are run with $N_{\text{h}} = 40$ harmonics and $N_{\text{t}} = 4\,000$ time instants. The value of ε is set to $\varepsilon = 1 \cdot 10^2\,\text{N·m}^{-1}$. Elements of validation of the choice of these numerical parameters are given in B.

3.2 Parametric study on the forcing amplitude A

In this study, the main parameter of interest is the amplitude of the forcing A that is being varied to observe peculiar behaviors of the dynamics response of the system. Discontinuous behaviors for the nonlinear resonances are identified on three ranges of values of A. All three discontinuous areas are displayed in Figs. 5, 6 and 7. For each figure, the levels of forcing A are written at the nonlinear resonances of the NFRC. In Figs. 6 and 7, the NFRC with the highest A of previous discontinuities are displayed (—) ($A = 2.5$ and $A = 18$).

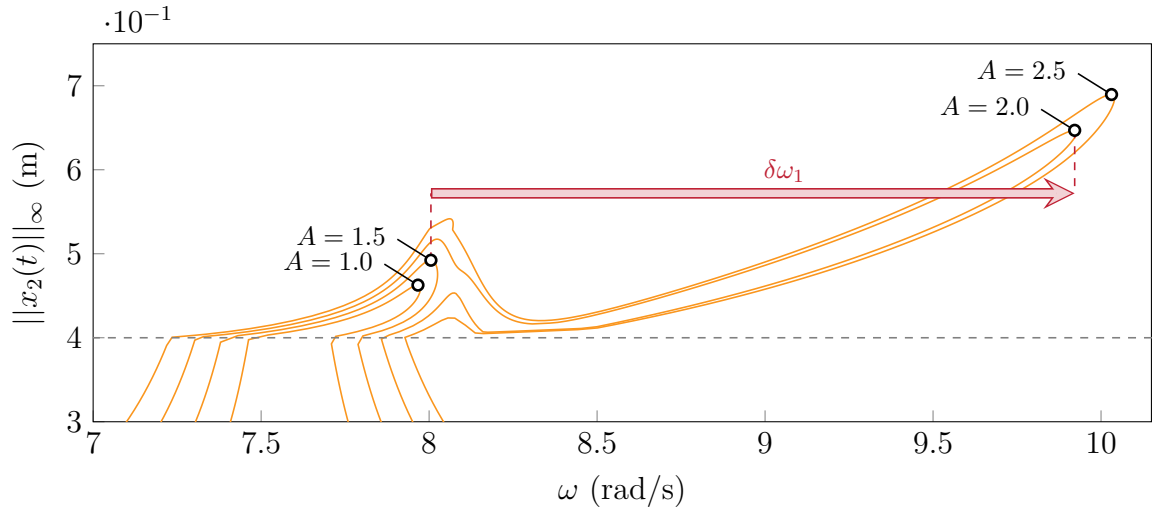

Figure 5. First resonance discontinuity of the NFRC with respect to A, NFRC with $A \in \{1.0, 1.5, 2.0, 2.5\}$ (—), g_0 (- -).

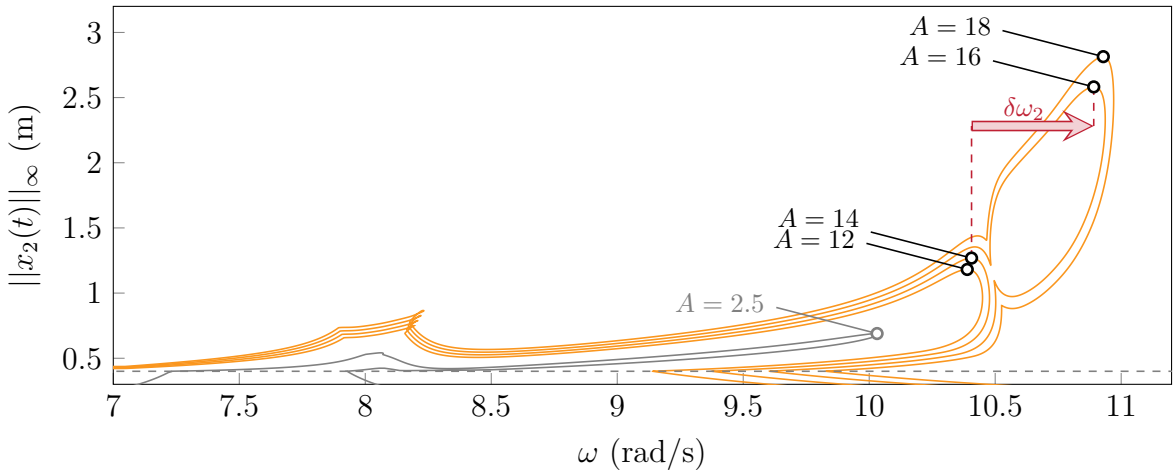

Figure 6. Second resonance discontinuity of the NFRC with respect to A, NFRC with $A \in \{12, 14, 16, 18\}$ (—), NFRC with $A \in \{2.5\}$ (—), g_0 (- -).

The resonance discontinuity represented in Fig. 5 occurs between $A = 1.5$ and $A = 2$, the second one in Fig. 6 between $A = 14$ and $A = 16$ and the third one in Fig. 7 between $A = 26$ and $A = 28$. This behavior appears to be the same for all three cases: a large branch of solutions suddenly appears after a threshold value of A. This phenomenon was already observed by Detroux *et al.* [13] and Mangussi *et al.* [15] for smooth nonlinearities. The authors showed that isolated branches were responsible of these discontinuities. Indeed, the threshold values of A are actually values of A for which the isolated branch connects itself back to the main NFRC.

3.3 Study of nonlinear normal modes of the system

3.3.1 Computation of nonlinear normal modes

Nonlinear normal modes allow to predict the frequency dependence of the nonlinear resonances. In the considered case NNM are able to provide valuable information in the areas near the resonance discontinuities. The nonlinear modal analysis of the system is displayed in Fig. 8 and yields a total of seven distinct NNM.

All NNM are obtained through different initializations. NNM 1 (—) is computed by initializing the continuation

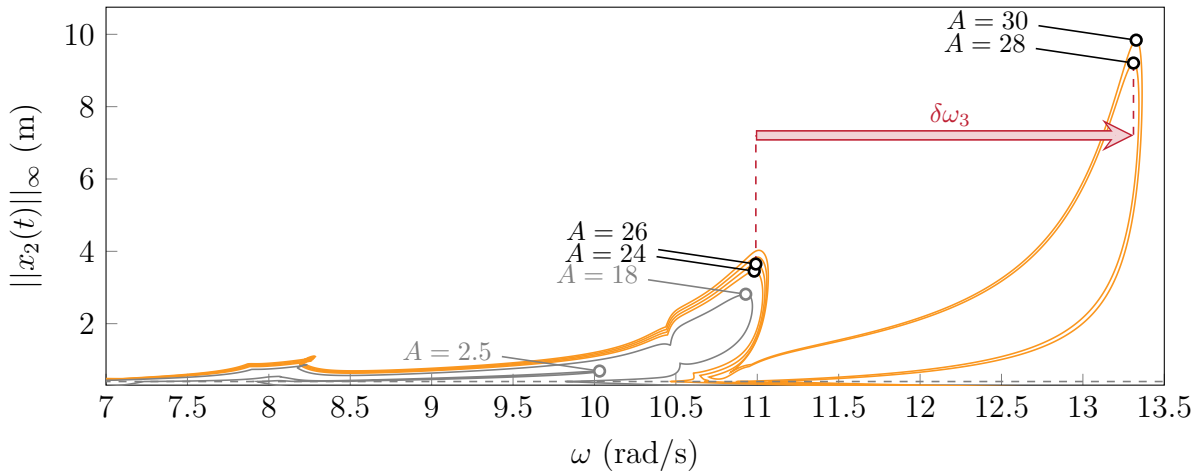

Figure 7. Third resonance discontinuity of the NFRC with respect to A, NFRC with $A \in \{24, 26, 28, 30\}$ (—), NFRC with $A \in \{2.5, 18\}$ (—), g_0 (- -).

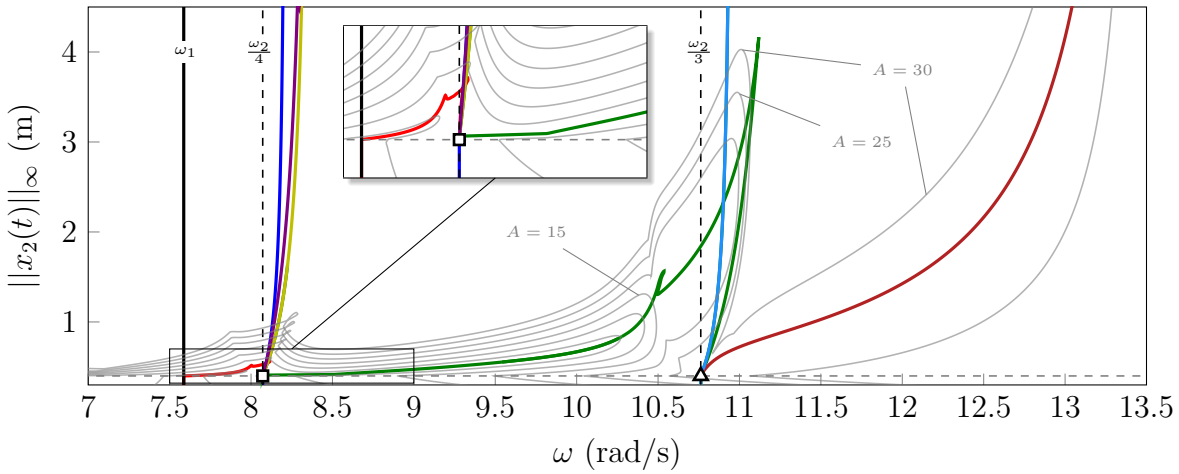

Figure 8. Nonlinear modal analysis on the nonlinear oscillator, NFRC with varying A (—), NNM 1 (—), NNM 2 (—), NNM 3 (—), NNM 4 (—), NNM 5 (—), NNM 6 (—), NNM 7 (—), ω_1 (—), fractions of ω_2 (- -), g_0 (- -), first singular point (◘), second singular point (△).

with the first linear mode shape on the first harmonic, in accordance with the excitation shape in the NFRC computations. Numerical issues occur when the continuation reaches the singular point (◘), causing the computation to stop. This point is at the intersection of the initial gap g_0 (- -) and the frequency $\omega = \frac{\omega_2}{4}$ (- -), it lies at the nonsmooth frontier between the linear and nonlinear domains. Modifying step control parameters in the continuation procedure leads to the discovery of NNM 2 (—), 3 (—) and 4 (—), all of them emerging from the singular point (◘). However, NNM 2, 3 and 4 do not seem to underlie any backbone curve of the forced responses. This multiplicity is closely related to the nonsmoothness of the problem of the boundary $\|x_2(t)\|_\infty = g_0$ as well as the notion of subdifferential [81]. Indeed, they all are nonlinear counterparts of the second linear mode of the system as shown in section 3.3.2. Due to the nonsmooth nature of the system studied, it is not expected that the nonlinear modal analysis presented in this work is exhaustive. Moreover, since HBM calculations are made with a fixed number of harmonics and fundamental pulsation, it is likely that some branches of periodic solutions have been missed.

In order to investigate if the backbone curve of the system is defined by some other nonlinear mode, a NNM is computed by initializing the continuation from the nonlinear resonance point of a NFRC that has already experienced

the first discontinuity, *i.e.* $A > 2$. The NNM 5 (—) is uncovered by this procedure and it accurately describes the backbone curve of the system between the first singular point (◘) and the second singular point (◬). The second singular point (◬) coincides with another particular frequency of the system: $\omega = \frac{\omega_2}{3}$. It is also located on the boundary delimiting linear and nonlinear responses. Continuation problems occur as well at this second singular point, preventing to compute the backbone curve past this point. In order to circumvent this difficulty, like for NNM 5 (—), an initialization on the nonlinear resonance past the third discontinuity, *i.e.* $A > 28$, is used for the computation of NNM 6 (—).

Finally, NNM 7 (—) is uncovered by initializing the continuation on the third harmonic with a pure $\mathbf{\Phi}_2$ mode shape. This is the nonlinear mode associated to ($\mathbf{\Phi}_2$, ω_2) but translated to $\omega = \frac{\omega_2}{3}$. By making further investigations, NNM 2 (—) is shown to be mainly composed of a response of the second mode shape $\mathbf{\Phi}_2$ with a fundamental frequency on the fourth harmonic, so that $4\omega \simeq \omega_2$. The latter is then also a translation of the second mode ($\mathbf{\Phi}_2$, ω_2) around $\omega = \frac{\omega_2}{4}$.

3.3.2 Singular points

The nonlinear modal analysis presented in section 3.3 underlines the very complex and highly nonlinear dynamics induced by the contact constraint. The nonlinear modal analysis allowed to detect two singular points (◘) (◬) for NNM. Indeed, all NNM go through at least of one these points. NNM 5 is even connected to both points at each of its ends. The intersection of all modes at these points suggests that the different branches of solutions emerge from the singular points. Since these points are located on the border between the linear and nonlinear domains—delimited by g_0—it is difficult to perform a bifurcation analysis due to the nonsmoothness of this boundary. In order to verify the hypothesis that all modes actually intersect in the resolution space, the solutions of each branch are investigated in the vicinity of the first singular point. As a way of looking at the whole responses and not only the vibratory amplitudes, solutions are decomposed in terms of modal contributions on each harmonic. For a single solution, the displacements are projected on the linear mode shapes at each time instant, such that

$$\gamma_j(t_i) = \mathbf{\Phi}_j^\top \mathbf{M}\mathbf{x}(t_i) \text{ for } i \in [\![1, N_\mathrm{t}]\!] \text{ and } j \in [\![1, n]\!]. \tag{27}$$

The periodic modal contributions $\gamma_j(t)$ are then expressed as truncated Fourier series of the form

$$\gamma_j(t) = \frac{a_0^{\gamma_j}}{2} + \sum_{k=1}^{N_\mathrm{h}} a_k^{\gamma_j} \cos(k\omega t) + b_k^{\gamma_j} \sin(k\omega t). \tag{28}$$

Finally, the Fourier coefficient $a_k^{\gamma_j}$ and $b_k^{\gamma_j}$ are retrieved to isolate the different harmonic contributions

$$c_0^{\gamma_j} = \left|a_0^{\gamma_j}\right| \quad \text{and} \quad c_k^{\gamma_j} = \sqrt{\left(a_k^{\gamma_j}\right)^2 + \left(b_k^{\gamma_j}\right)^2} \quad \forall k \in [\![1, N_\mathrm{h}]\!]. \tag{29}$$

All of the $c_k^{\gamma_j}$ quantities are displayed in Fig. 9 for each NNM near the first singular point.

In Fig. 9, all five NNM that go through the first singular point (◘) on the NFRC in Fig. 8 are also experiencing the exact same overall dynamics response. It is a pure $\mathbf{\Phi}_2$ mode shape on the fourth harmonic. A slight modulation of the response by the first harmonic on NNM 5 is detected, however it is small relatively to the fourth harmonic. This observation confirms that all NNM coincide in the resolution space. It strongly supports the hypothesis that all NNM emerge from the singular point, making it difficult to follow a particular branch without specific developments. Moreover, the boundary where singular points are located is nonsmooth, preventing the application of a classical branch switching strategy [52] because of the discontinuous nature of derivatives.

3.3.3 Super-harmonic nonlinear normal modes

NNM 2 (—), 3 (—) and 4 (—) do not seem to underlie any backbone curve of the system for the given monoharmonic forcing. As a last step of investigation on the NNM, the three NNM are compared in terms of overall dynamics to uncover their characteristics. As a way of performing this comparison, a solution of each NNM is extracted at constant total energy of $E_\mathrm{tot} = 1\,\mathrm{J}$. The time signals and multiharmonic modal contributions are displayed in Fig. 10.

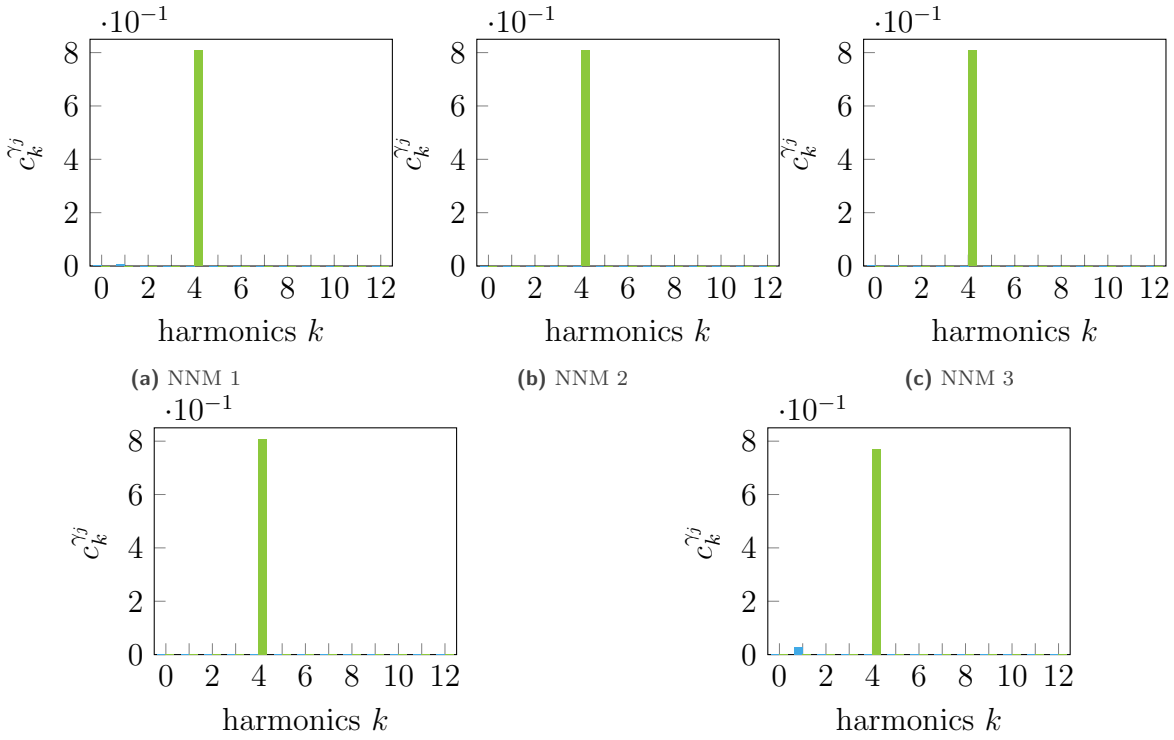

(a) NNM 1 **(b)** NNM 2 **(c)** NNM 3

(d) NNM 4 **(e)** NNM 5

Figure 9. Multiharmonic modal contributions at the first singular point (□) for each NNM, mode 1 ($j = 1$) (▭), mode 2 ($j = 2$) (▭).

The dynamics uncovered in Fig. 10 show that all three NNM have different periodicities. Indeed, the NNM 2 has a fundamental pulsation of 4ω, the NNM 3 has a fundamental pulsation of 2ω and the NNM 4 is synchronous with ω. All of them also share a strong contribution of the second mode on the fourth harmonic. This suggests that these modes are associated with the second mode of the system ($\mathbf{\Phi}_2$, ω_2). It also justifies the fact that these modes do not seem to be involved in the forced response calculations since the forcing only excites the first linear mode shape on the first harmonic.

3.4 Computation of isolated branches with a Melnikov analysis

In section 3.3, an exhaustive nonlinear modal analysis showed the existence of numerous branches of autonomous solutions on the frequency range of interest. These nonlinear modes already provide qualitative information about the system's dynamics, especially concerning the nonlinear resonances. The aim of the current section is to provide supplementary information on the forced response of the system given the knowledge of the solutions of the different nonlinear modes by using the Melnikov analysis.

The Melnikov analysis allows to state if periodic solutions in the forced damped configuration exist in the vicinity of each solution of each NNM noted $\mathbf{x}_c$. In order to make those predictions, one must examine the sign of the function $\overline{\mathcal{M}}^{1:1}(A, \mathbf{f}_{ex}, \mathbf{C}, \mathbf{x}_c)$, referred to as the energy balance function (EBF), defined by

$$\overline{\mathcal{M}}^{1:1}(A, \mathbf{f}_{ex}, \mathbf{C}, \mathbf{x}_c) = \left|W^{1:1}(A, \mathbf{f}_{ex}, \mathbf{x}_c)\right| - \left|\mathcal{R}(\mathbf{C}, \mathbf{x}_c)\right|. \tag{30}$$

The sign of this function directly refers to the energy principle given in section 2.5. For this study, only NNM 1, 3 and 6 are considered since these modes are the only NNM being composed of a strong first harmonic contribution. Indeed, since $\left|W^{1:1}(A, \mathbf{f}_{ex}, \mathbf{x}_c)\right|$ directly depends on $\mathbf{a}_c^1$ and $\mathbf{b}_c^1$, if these quantities are null or small compared to

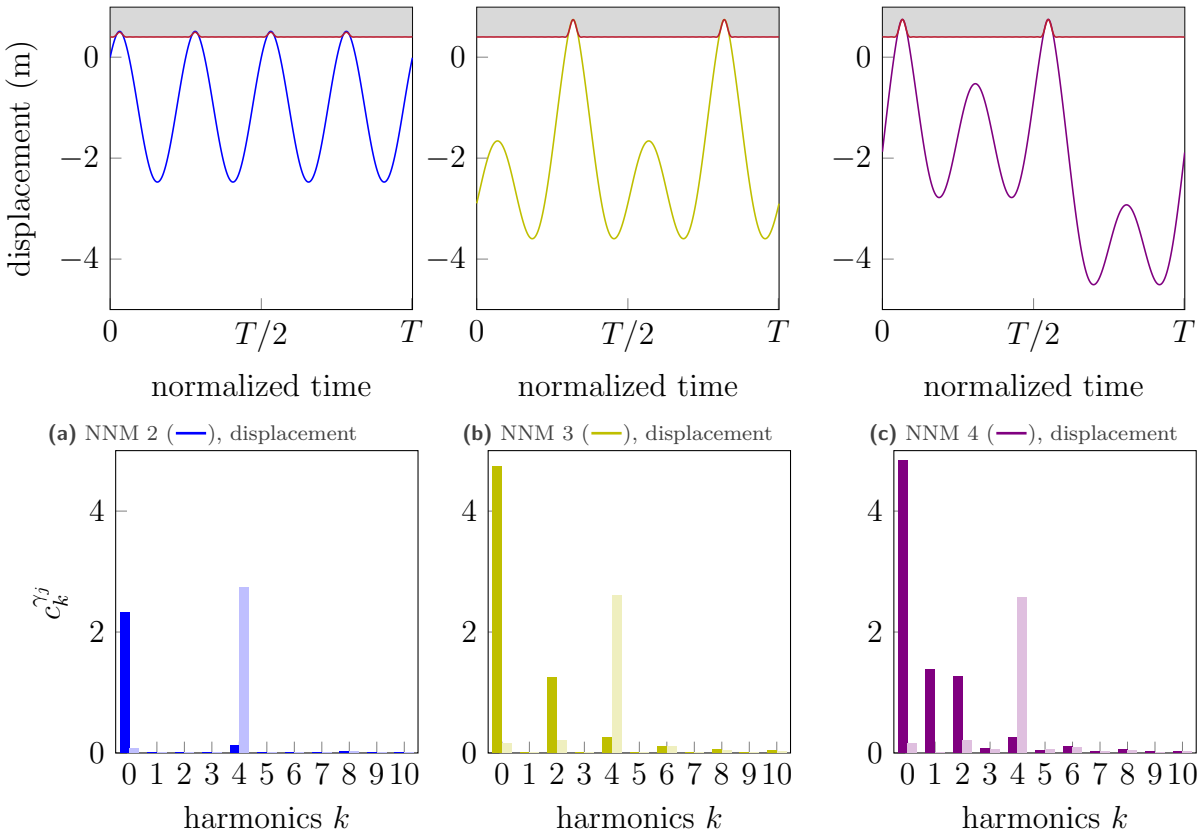

(a) NNM 2 (—), displacement **(b)** NNM 3 (—), displacement **(c)** NNM 4 (—), displacement

(d) NNM 2 (—), multiharmonic modal contributions **(e)** NNM 3 (—), multiharmonic modal contributions **(f)** NNM 4 (—), multiharmonic modal contributions

Figure 10. Comparison of solutions at $E_{\text{tot}} = 1\,\text{J}$ of NNM 2, 3 and 4, $x_2(t)$ (—), (—), (—), obstacle (▭), mode 1 ($j = 1$) (▬), (▬), (▬), mode 2 ($j = 2$)(▬), (▬), (▬).

other harmonics, then Melnikov's criterion states that no solution can persist for an harmonic forcing on the first harmonic. Indeed, the work term $\left|W^{1:1}(A, \mathbf{f}_{\text{ex}}, \mathbf{x}_{\text{c}})\right|$ would be null or small compared to the resistance $|\mathcal{R}(\mathbf{C}, \mathbf{x}_{\text{c}})|$. This is consistent with the observations that NNM 2, 3, 4 and 7 do not contribute to the forced responses. It can be attributed to the fact that their harmonic content are mainly composed of the fourth and third harmonics. These superharmonic modes could still be studied by Melnikov analyses if the forcing were on the dominant harmonics of their response, however for the sake of concision only forcings along the first harmonic are retained for this article.

In the following, all three resonance discontinuities are addressed by Melnikov analyses in their respective ranges of forcing amplitudes A (around $A = 1.75$, $A = 15$ and $A = 27$).

3.4.1 First resonance discontinuity

For a given forcing amplitude $A = 1$, the EBF is represented in Fig. 11a for the two NNM of interest : 1 and 5. It is depicted as a function of ω for the sake of readability. The sign of $\overline{\mathcal{M}}^{1:1}$ is also superimposed over the NNM on the NFRC graph in Fig. 11b.

It is observed in Fig. 11 that the EBF becomes positive for both NNM on two non-contiguous frequency ranges. For the NNM 1 (—), this frequency range is easily attributed to the main NFRC previously computed in section B. Moreover, a relatively good level of precision is obtained concerning the existence of periodic solutions on NNM 1. Indeed, the nonlinear resonance matches with the area where the EBF becomes negative (*i.e.* the NNM goes from thick to thin line). However, the second area where the EBF is positive belongs to the NNM 5 (—) and it

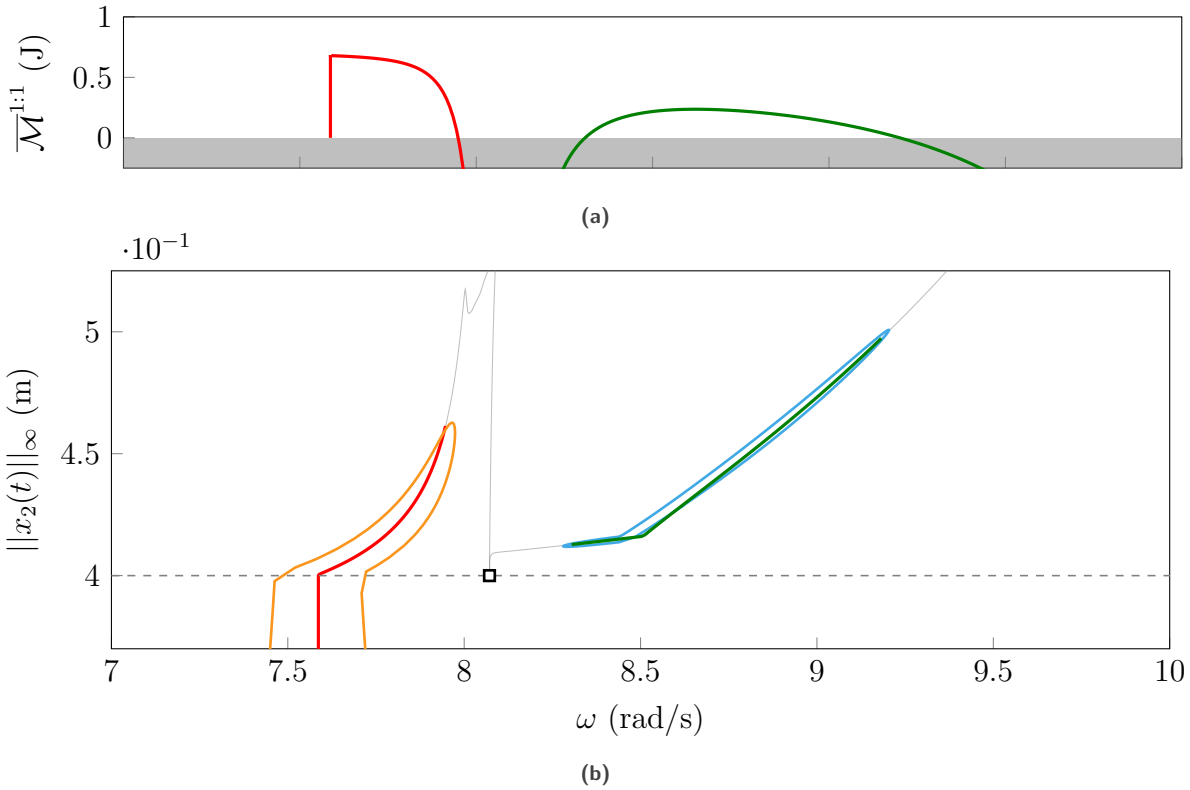

Figure 11. Result of the Melnikov analysis for $A = 1$, (a) EBF, (b) NFRC, NNM 1 (—), NNM 5 (—), NFRC (—), isolated branch (—), two periodic orbits persist ($\overline{\mathcal{M}}^{1:1} > 0$) (▬), no periodic orbits persist ($\overline{\mathcal{M}}^{1:1} < 0$) (—), g_0 (- -), first singular point (□).

appears to be isolated from the main NFRC. In order to verify if Melnikov's criterion successfully predicted the existence of solutions, a continuation procedure is started using a NNM autonomous solution as a first guess. This computation allows to capture an isolated branch (—) that perfectly coincides with the frequency range predicted by the Melnikov analysis.

By doing further Melnikov analyses with various values of A, it is observed that the first discontinuity area actually corresponds to a merge between a family of isolated branches and the main NFRC for the threshold value of $A = 1.8$. The isolated branches are obtained by identifying areas where the EBF is positive and starting a continuation strategy in these areas. The full view of the main NFRC and the isolated branches is represented in Fig. 12 from $A = 1$ to $A = 2.4$.

In fact, the merge of the isolated branch with the main NFRC happens when the two branches start to overlap in terms of frequency. Since the isolated branch and the main NFRC emerge from different NNM, the singular point plays a central role in this discontinuity. Should periodic solutions exist sufficiently close to the singular point of both sides, then the isolated branch suddenly merges with the main NFRC. This happens for a relatively high value of the amplitude A because the solutions on the different NNM near the singular point are composed of a pure fourth harmonic contribution. This strong contribution of the fourth harmonic is responsible of a drop in the value of $\left|W^{1:1}\right|$, causing the EBF to become locally negative near the singular point. In order to illustrate this phenomenon, the Melnikov analysis for $A = 2$ (*i.e.* just after the merge) is displayed in Fig. 13.

The Melnikov analysis represented in Fig. 13 does not precisely predict the merge of the branch because the EBF is negative on a small frequency range around $\omega = \frac{\omega_2}{4}$. However, this test case pushes the methodology to its limits since the behavior of the system is highly sophisticated in this area. As stated earlier, it is found that the

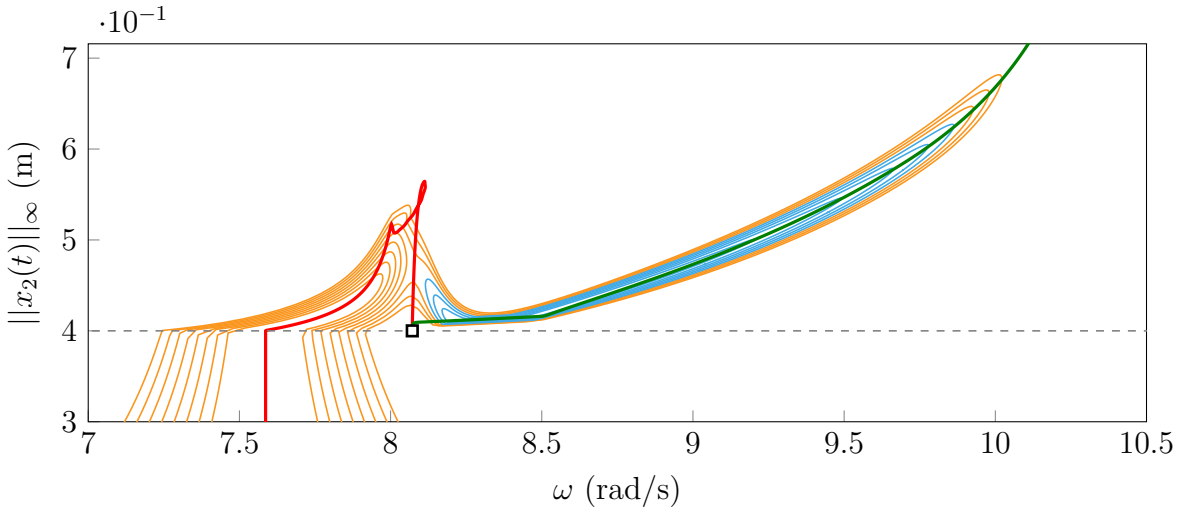

Figure 12. Merge of the first isola family, NFRC from $A = 1$ to $A = 2.4$ by steps of 0.2 (—), isolated branches from $A = 1$ to $A = 1.8$ by steps of 0.2 (—), NNM 1 (—), NNM 5 (—), g_0 (- -), first singular point (◘).

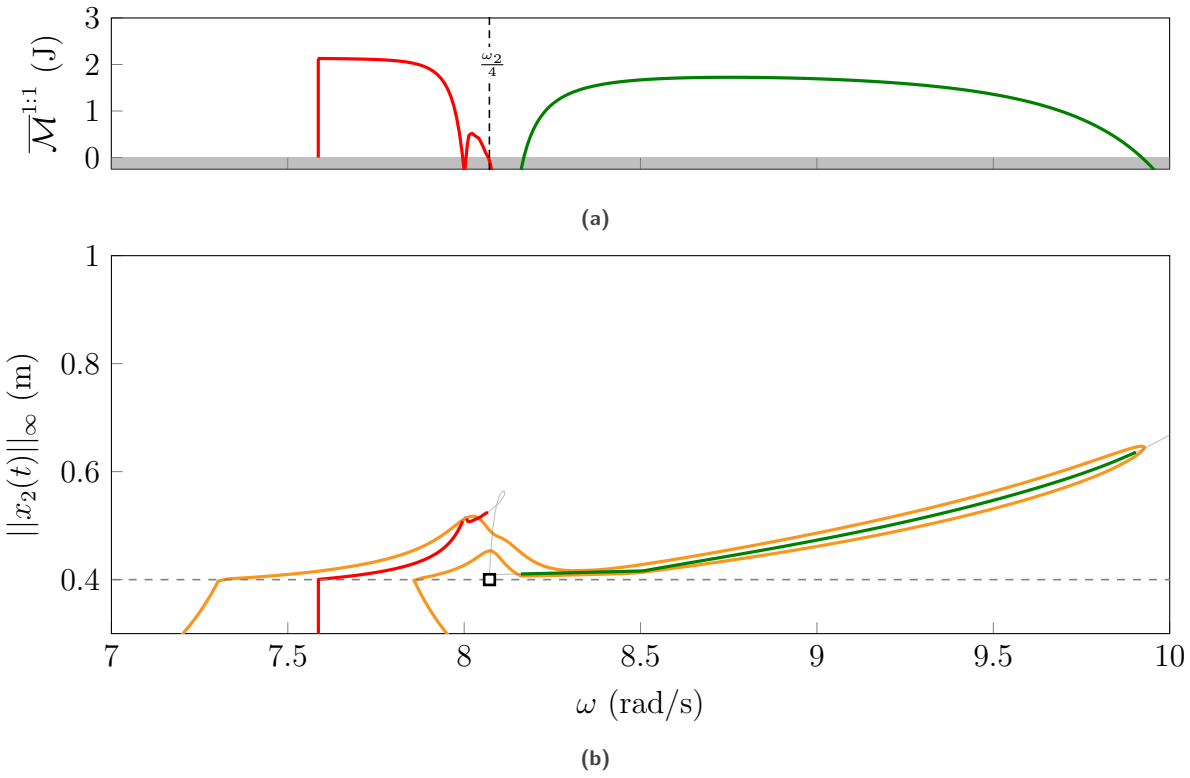

Figure 13. Result of the Melnikov analysis for $A = 2$, (a) EBF, (b) NFRC, NNM 1 (—), NNM 3 (—), NFRC (—), isolated branch (—), two periodic orbits persist ($\overline{\mathcal{M}}^{1:1} > 0$) (—), no periodic orbits persist ($\overline{\mathcal{M}}^{1:1} < 0$) (—), g_0 (- -), first singular point (◘).

EBF becomes negative for both modes in the vicinity of the singular point. Even if near the sensitive points the methodology struggles to make a precise prediction, the nonlinear resonance is still accurately identified along NNM

5 (—).

3.4.2 Second resonance discontinuity

In this section, the second resonance discontinuity is investigated. Contrary to the the first discontinuity, the second discontinuity occurs along a single NNM. As shown by the Melnikov analysis displayed in Fig. 14 for an amplitude $A = 12$, the resonance discontinuity takes place around a local peak of amplitude of the NNM 5 (—). Thanks to the calculation of the resistance term $\mathcal{R}$ it is possible to identify a raise in terms of dissipated energy on this peak, not shown in this article for the sake of brevity. This has the consequence of preventing periodic solutions to exist on the peak while solutions can more easily persist on either side of it. The latter is then responsible for the disconnection of branches of solutions from either sides of the peak identified in Fig. 14.

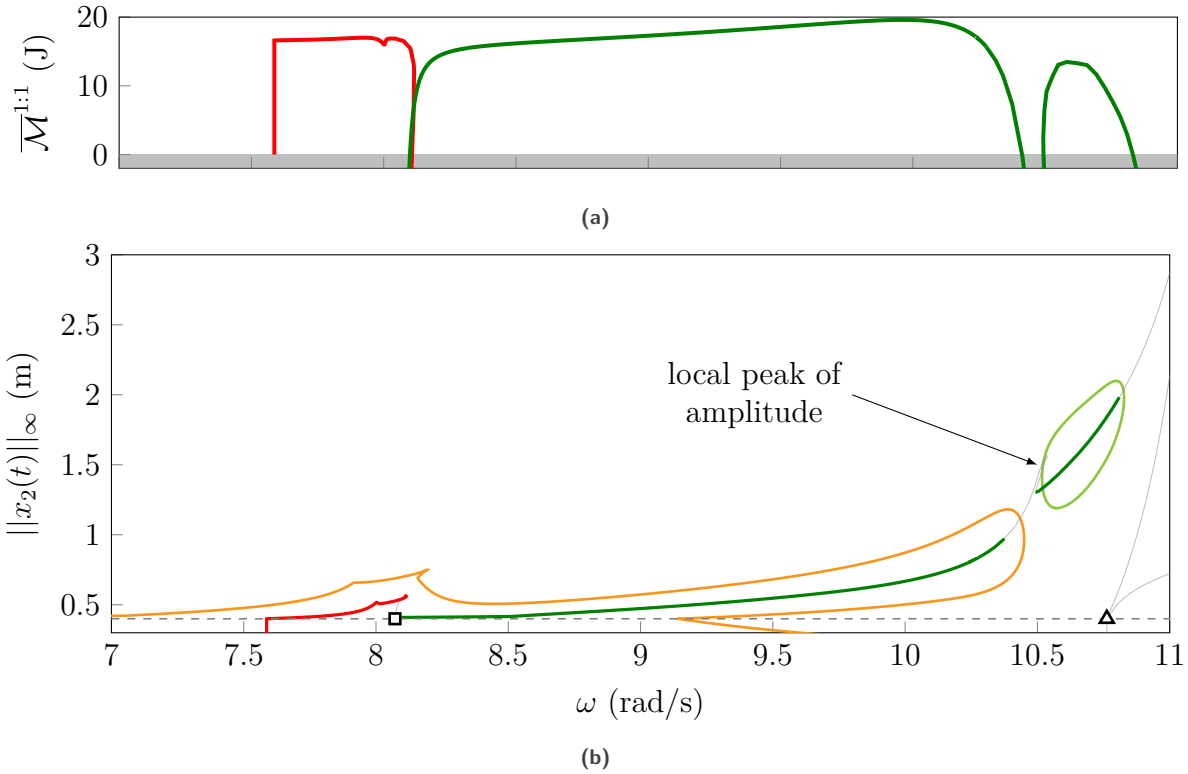

Figure 14. Result of the Melnikov analysis for $A = 12$, NNM 1 (—), NNM 3 (—), NFRC (—), isolated branch (—), two periodic orbits persist ($\overline{\mathcal{M}}^{1:1} > 0$) (▬), no periodic orbits persist ($\overline{\mathcal{M}}^{1:1} < 0$) (—), g_0 (- -), first singular point (□), second singular point (△).

Once again, the Melnikov analysis predicts a frequency range where periodic solutions should bifurcate from the NNM for this level of forcing, however the main NFRC does not account for this frequency range. In the same manner as in section 3.4.1, an isolated branch (—) is identified. This procedure is used at multiple amplitude levels in order to obtain Fig. 15.

3.4.3 Third resonance discontinuity

Finally, the third area of discontinuity is investigated through the same procedure as the first two discontinuities. The third discontinuity is analogous with the first one and is therefore not presented with the same level of detail.

Firstly, the Melnikov analysis represented in Fig. 16 is able to predict the existence of an isolated branch for $A = 5$ which is a relatively low amplitude of forcing. Indeed, since the merge of the associated isolated branch occurs

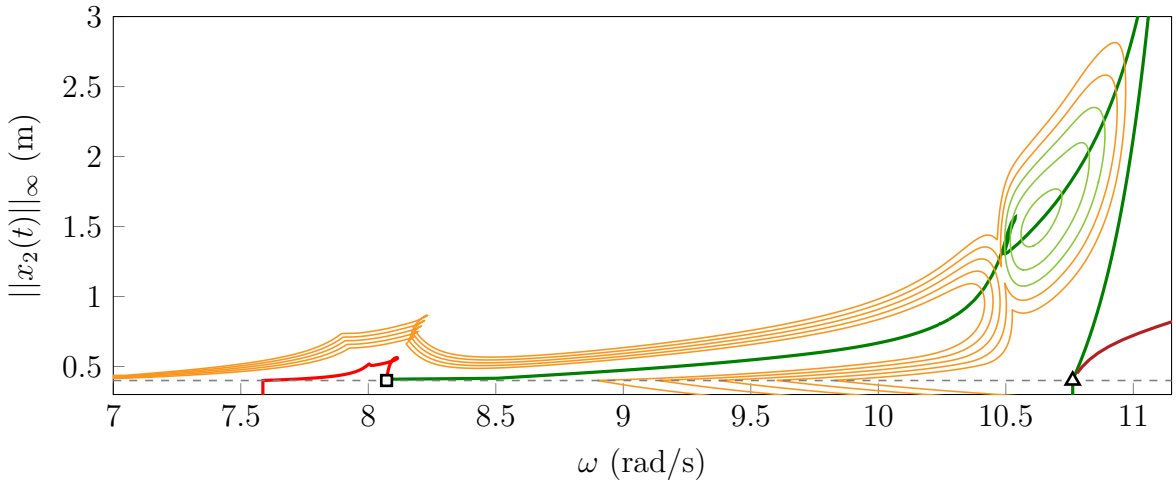

Figure 15. Merge of the second isola family, NFRC from $A = 10$ to $A = 18$ by steps of 2 (—), isolated branches from $A = 10$ to $A = 14$ by steps of 2 (—), NNM 1 (—), NNM 5 (—), NNM 6 (—), g_0 (- -), first singular point (□), second singular point (△).

between $A = 26$ and $A = 28$, this shows that the family of isolas appears for much lower values than the threshold value of the merge. For example, the appearance of the third family of isolas (—) precedes the appearance of the second one (—).

By applying Melnikov analyses on the amplitude range $A = 5$ to $A = 30$ by steps of 5, the NFRC and associated isolated branches are obtained in Fig. 17. The merge occurs in the vicinity of the second singular point (△), in the same way that the first singular point (□) is close the merge of area of the first discontinuity. In the end, a really good agreement is found between the predicted nonlinear resonances through nonlinear modal analysis and the actual NFRC computations, even for isolated resonances.

3.4.4 Overall dynamics of the system

As a way of displaying the evolution of the nonlinear resonance with respect to A on the whole range of amplitudes, going from $A = 1$ to $A = 30$, the evolution of the stiffening of the nonlinear resonance and the evolution of its amplitude are respectively depicted in Figs. 18a and 18b. The stiffening $\Delta\omega(A)$ refers to the frequency shift of the resonance and is computed following $\Delta\omega(A) = \omega_{\text{res}}(A) - \omega_1$ where $\omega_{\text{res}}(A)$ is the pulsation where the amplitude of nonlinear response is maximum at a given forcing amplitude A.

All three discontinuities of nonlinear resonances for the main NFRC (—●—) are identified in Fig. 18 by both amplitude and frequency jumps (→). These jumps are critical as they cause sudden and significant increases in terms of response amplitude with a small increase of the forcing amplitude. The use of the Melnikov analysis allows to predict the possibly isolated nonlinear resonance (—●—). Finally and with the use of the energy principle, all isolated branches are computed and each depicted according to the family to which they belong (first (—●—), second (—●—) and third (—●—)) in Fig. 18. The latter allows to see the amount of information missed by typical NFRC continuation techniques (—●—). Indeed, the use of Melnikov analyses shows the appearance of remote isolated nonlinear resonances for a wide range of forcing amplitudes A. The computation of all isolated branches shows that the predictions made through Melnikov analyses are very accurate. Indeed, the nonlinear resonance is precisely located whether it belongs to main NFRC (—●—) or to isolated branches (—●—) (—●—). The level of accuracy achieved is such that there is no need to compute the actual isolated branches of solutions if the sought information is the locus of the nonlinear resonance at a given forcing amplitude A.

In Fig. 19, the system's dynamics response is displayed for several levels of forcing A. Figure 19 also recalls the fact that the third isola family (—) appears before the second family (—). Moreover, it underlines that the isolated resonances (—) are very remote from the resonances of the main NFRC.

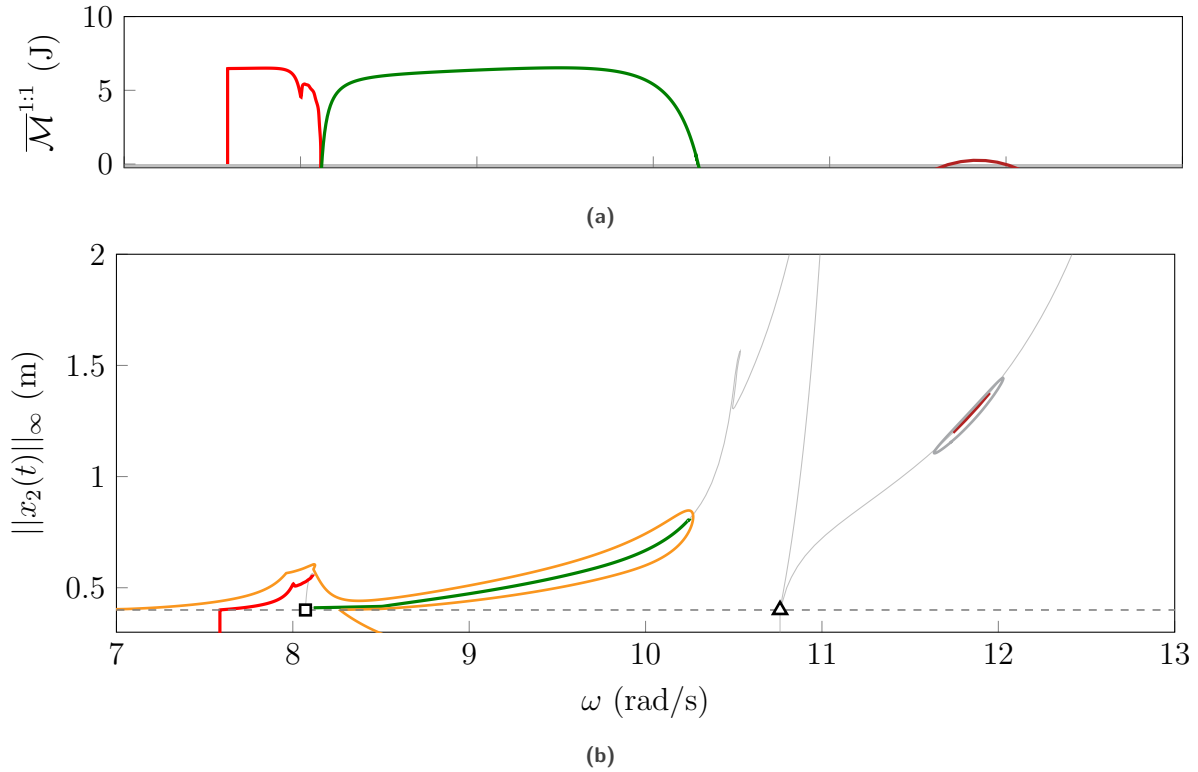

Figure 16. Result of the Melnikov analysis for $A = 5$, (a) EBF, (b) NFRC, NNM 1 (—), NNM 3 (—), NNM 6 (—), NFRC (—), isolated branch (—), two periodic orbits persist ($\overline{\mathcal{M}}^{1:1} > 0$) (—), no periodic orbits persist ($\overline{\mathcal{M}}^{1:1} < 0$) (—), g_0 (- -), first singular point (□), second singular point (△).

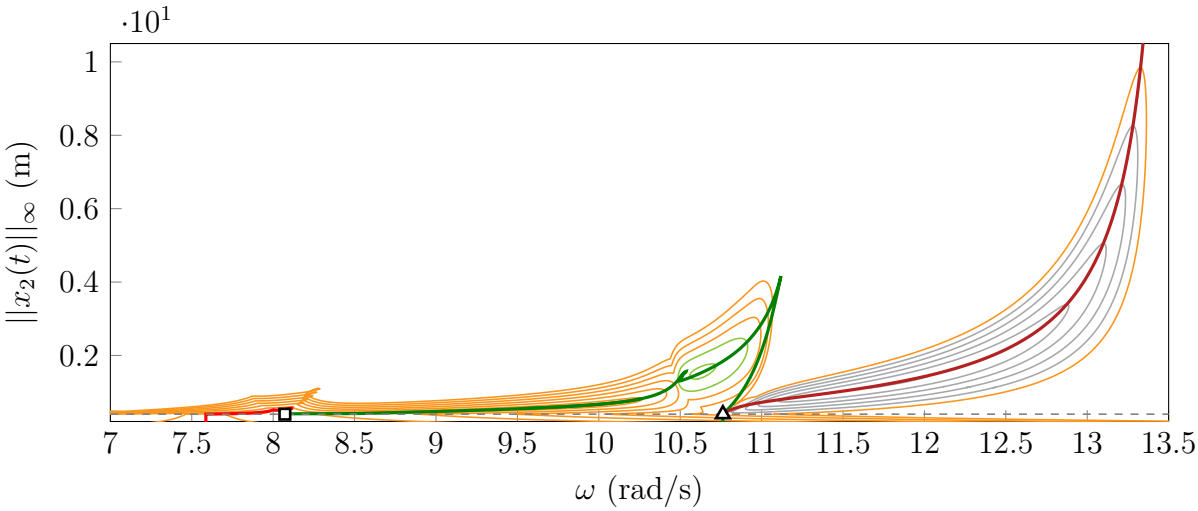

Figure 17. Merge of the third isola family, NFRC from $A = 5$ to $A = 30$ by steps of 5 (—), isolated branches for $A = 10$ and $A = 15$ (—), isolated branches from $A = 5$ and $A = 25$ by steps of 5 (—), NNM 1 (—), NNM 5 (—), NNM 6 (—), g_0 (- -), first singular point (□), second singular point (△).

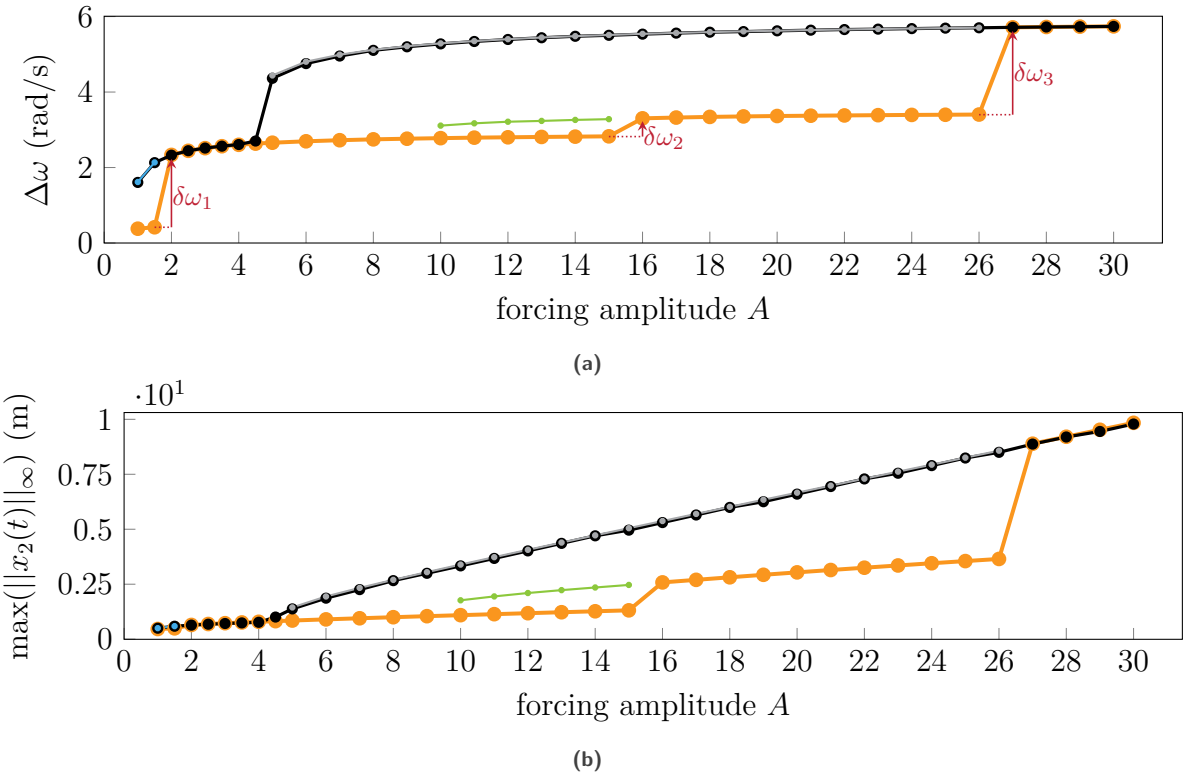

Figure 18. Evolution of the nonlinear resonances with A, (a) stiffening effect, (b) maximum displacement, main NFRC (—●—), prediction by Melnikov (—●—), first isola family (—●—), second isola family (—●—), third isola family (—●—).

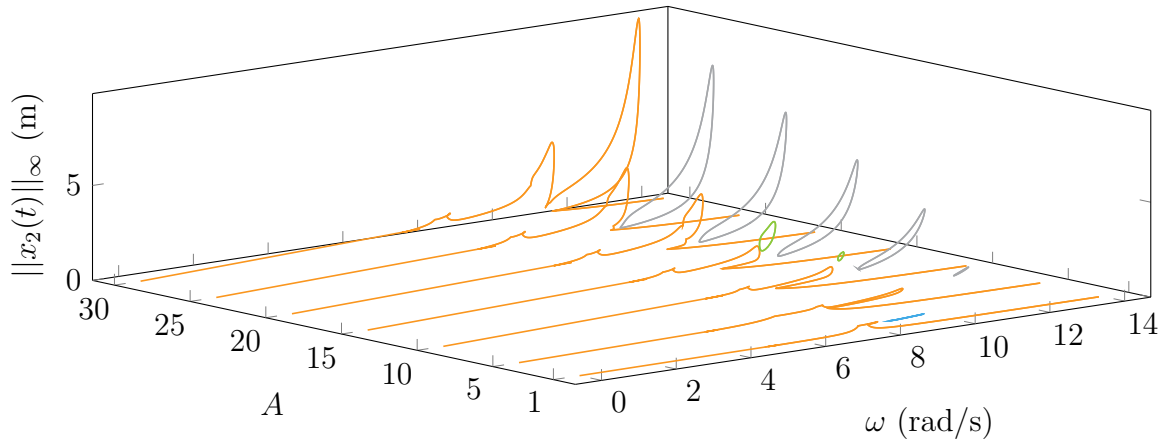

Figure 19. Full view of the system NFRC including isolated branches, main NFRC (—), isolated branches (—) (—) (—).

3.5 Comparison with a reference time-marching strategy

As a step of numerical verification of the results presented in section 3.4, time-marching simulations are run in order to verify that the isolated solutions found by HBM are also solutions for time-domain paradigm strategies. The entire frequency range is discretized into steps of $\mathrm{d}\omega = 0.005\,\mathrm{rad{\cdot}s^{-1}}$ and a constant speed simulation is run at each point by using the closest HBM solution as initial conditions for the time-domain solver. The amplitude chosen for this comparison is $A = 15$ where two families of isolated branches coexist. The results are also superimposed with a

Melnikov analysis in Fig. 20.

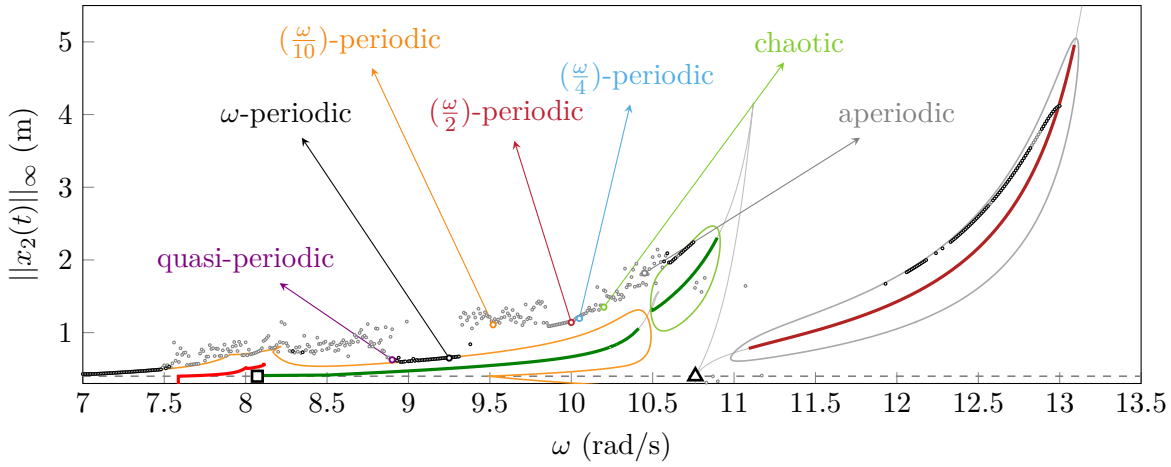

Figure 20. Melnikov analysis superimposed with time-marching results for $A = 15$, NFRC (—), isolated branches (—) (—), NNM 1 (—), NNM 5 (—), NNM 6 (—), two periodic orbits persist ($\overline{\mathcal{M}}^{1:1} > 0$) (▬), no periodic orbits persist ($\overline{\mathcal{M}}^{1:1} < 0$) (—), g_0 (- -), first singular point (□), second singular point (△), ω-periodic time-marching results (○), underharmonic and aperiodic time-marching results (○).

The superimposition of the time-marched solutions in Fig. 20 reveals a sophisticated behavior of the system. Since no periodicity condition is imposed on the TI solutions, a large part of the periodic solutions found by HBM do not remain on the same orbit after being integrated over a hundred periods. In order to observe the dynamics of the solutions that are not ω-periodic, the Poincaré maps [82]–a commonly used analysis tool in nonlinear dynamics–of some of the solutions obtained by TI are built. The corresponding TI solutions are highlighted in Fig. 20. For a given orbit, a Poincaré map is characterized by a set of points corresponding to readings of the state of the system at times separated by a regular interval T, associated with the period of the excitation. In the given configuration, the couples $(x_2(t + kT),\ \dot{x}_2(t + kT))\ \forall k \in [\![20\,000; 60\,000]\!]$ are taken, which correspond to the last forty thousand periods of integration over a total time of sixty thousand periods. The integration time is only extended to sixty thousand periods on the few TI points for which the Poincaré map is built. On Poincaré maps, a periodic solution of fundamental period mT is identified when the section contains exactly m distinct points. The quasi-periodic solutions are characterized by a continuous closed curve. The Poincaré map of a chaotic solution is characterized by clusters of disordered points with a fractal appearance, also known as a strange attractor. Finally, no distinctive pattern can be observed in the case of a solution that is not periodic (aperiodic). The Poincaré maps of the selected points are represented in Fig. 21 and three categories of solutions are distinguished:

- the solution is periodic with the same periodicity as the excitation (○): it is possible to compare it with the frequency-domain solutions,
- the solution is periodic but with a periodicity different from that of the excitation: it belongs to a period-doubled branch (○), period-quadrupled (○) or even of more important period (○),
- the solution reaches a quasi-periodic (●), chaotic (●) or aperiodic (●) regime, these areas appear as diffuse clouds of points in Fig. 20.

Among these three categories, the first one is the only one of interest for the comparison of the two paradigms. Therefore, it is represented by black dots (○) in Fig. 20. Among the solutions of fundamental period ω, not all are of interest: some solutions return to the linear domain ($\|x_2(t)\|_\infty < g_0$) and are thus not relevant for the study of the nonlinear response. On the nonlinear points where a ω periodicity is detected, a fairly good agreement is observed in terms of vibrational amplitude. Around the nonlinear resonance of the third family of isolated branches of solutions (—), a slight amplitude discrepancy is observed. Nevertheless, the TI simulations still account for the high amplitude dynamics of the isolated nonlinear resonance.

The periodicity analysis allows to highlight that periodic solutions persist on several portions of the main NFRC,

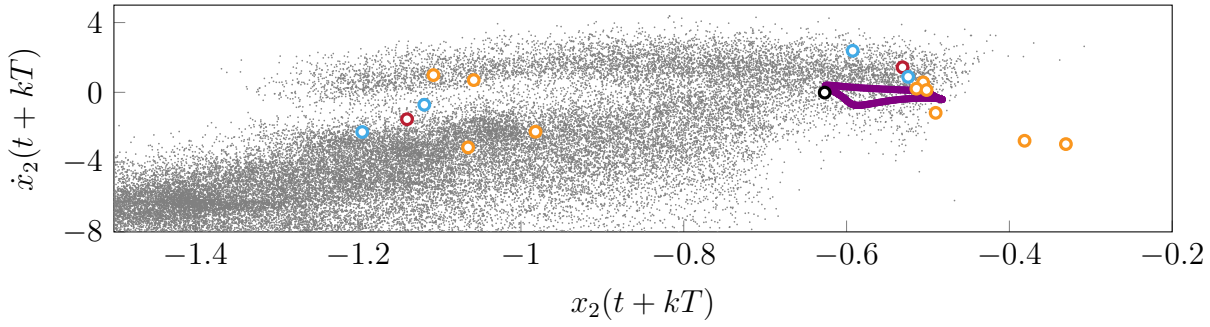

(a) periodic, quasi-periodic and aperiodic solutions

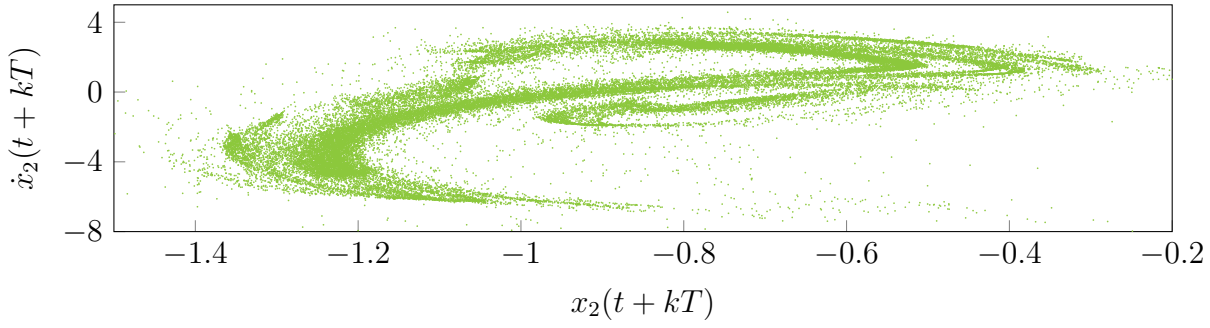

(b) chaotic solution

Figure 21. Poincaré maps of the different categories of solutions, ω-periodic solution (●), $(\frac{\omega}{2})$-periodic solution (●), $(\frac{\omega}{4})$-periodic solution (●), $(\frac{\omega}{10})$-periodic solution (●), quasi-periodic solution (●), chaotic solution (●), aperiodic solution (●).

but also on each isolated branch. Since contact treatments are radically different, it consolidates the idea that these isolated branches are composed of both stable and unstable solutions. Indeed, the difference in contact treatment between HBM and time-marching simulations represents a perturbation on the system. If the time-marching simulation remains on the same periodic orbit as the HBM then the perturbation linked to the difference of contact treatment has completely vanished, thus the solution can be considered to be locally stable. In order to finely detect bifurcations points and stable branches, a dedicated stability analysis would be needed but it exceeds the scope of this paper. Very recently, Colaïtis and Batailly [39] proposed an approach in order to perform stability analyses in the framework of contact interactions and HBM on both phenomenological and industrial models for a regularized and filtered contact law. Nevertheless, the nonsmooth nature of DLFT-HBM brings numerous difficulties to the use of the classical methodologies for the analysis of local stability: $\frac{\partial \mathbf{f}_{\mathrm{nl}}}{\partial \mathbf{x}}$ is only piecewise continuous in the time domain which yields derivatives with spurious oscillations around discontinuities when derivative signals are truncated to the number of harmonics of the HBM. Using the derivatives of the contact forces with respect to the displacement field $\mathbf{x}$ and the velocity field $\dot{\mathbf{x}}$ ($\frac{\partial \mathbf{f}_{\mathrm{nl}}}{\partial \mathbf{x}}$ and $\frac{\partial \mathbf{f}_{\mathrm{nl}}}{\partial \dot{\mathbf{x}}}$), as required by Floquet's theory, then leads to monodromy matrices of poor quality, preventing an accurate stability analysis. In fact, new developments are needed in order to be able to rigourously state on the local stability of periodic orbits for highly nonlinear nonsmooth systems, such as vibro-impact applications. The extension of Floquet's theory to nonsmooth problems would also allow for the use of new techniques relying on Melnikov-type studies for the evaluation of local stability of periodic orbits [83].

3.6 Partial conclusion

The phenomenological system studied in section 3 revealed highly nonlinear phenomena. The isola detection procedure allowed to explain the resonance discontinuities initially uncovered by classical continuation techniques. These isolas being of higher amplitudes and featuring higher stiffening effects than the resonances of the main NFRC, it supports the idea that isolated branches should systematically be searched for in order to ensure that all

solutions are captured. As these phenomena were already observed on industrial configurations [14] and experimental setups [13], design procedures should account for these nonlinear behaviors in order to properly estimate the maximum stresses undergone by the systems. As a way of providing a proof of applicability to high-dimensional industrial systems of the proposed isola detection procedure, the latter is applied to the NASA rotor 37 industrial blade model in a forced response configuration.

4 Industrial application: NASA rotor 37 compressor blade

The NASA rotor 37 industrial blade model is chosen for this test case because its open geometry [1] allows for results reproductibility. The NASA rotor 37 is a 36-blade transsonic axial compressor stage designed at NASA's Lewis research center in the late 1970s [84]. It was previously used as a test case in the field of computational fluid dynamics [85, 86, 87, 88] and more recently in structural dynamics for the analysis of rubbing interactions [34, 36, 38, 39].

4.1 Blade model

The mesh is composed of 5745 nodes for a total of 1800 quadratic pentahedron elements. The root of the blade is considered clamped, making the total size of the model of 16524 dof. Since the rotor 37 is made of a maraging steel grade 200 alloy, the mechanical properties of a 18-Ni 200-maraging alloy [34] are retained for the simulations, the Young's modulus, density and Poisson's ratio are given in the table 2. The rotor and the mesh of a single blade are depicted in Fig. 22.

Young's modulus E	Density ρ	Poisson coefficient ν
180 GPa	8,000 kg·m^{-3}	0.3

Table 2. Material properties retained for 18-Ni 200-maraging steel alloy.

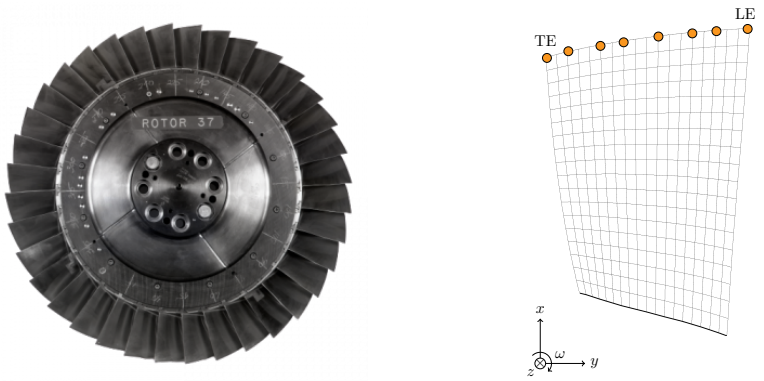

(a) **(b)**

Figure 22. NASA rotor37 [89], (a) blisk, (b) mesh.

A reduced-order model is produced using the Craig-Bampton strategy [90]. $\eta = 10$ internal modes and $n_b = 8$ evenly-spaced boundary nodes along the blade-tip are retained. These parameters are retrieved from previously published studies [34, 38, 39] and convergence with respect to both the mesh and the reduced-order model were thoroughly checked beforehand. The blade's structural damping is represented through modal damping, using the modal coefficients $\xi_{1-2} = 1 \cdot 10^{-3}$ for the the first bending mode (1B) and the first torsional mode (1T). All other modes are damped with a higher modal damping rate of $\xi_{3+} = 5 \cdot 10^{-3}$. The first bending mode of the blade is

[1] available at https://lava-wiki.meca.polymtl.ca/public/accueil#modeles_numeriques

the mode of interest in the study and it is located at $\omega_{1B} = 5{,}272.3\,\mathrm{rad{\cdot}s^{-1}}$. For this study, a single blade is used so that the configuration is the same as in the literature [34, 38, 39], it also allows to keep the computing times reasonable. The first eigenfrequencies of the blade are given in table 3. In this section, all NFRC graphs represent the amplitude of the radial displacements at the leading edge $r_1(t)$.

mode $\bullet$	1B	1T	2B	4	5
$\omega_\bullet$ (rad·s^{-1})	5,272.9	15,770.6	19,098.6	29,586.4	36,141.3
f (Hz)	839.2	2,510.0	3,039.6	4,708.8	5,752.1

Table 3. First eigenfrequencies of the blade of the rotor 37.

4.2 Contact scenario

In order to easily transpose the methodology applied in section 3 to the rotor 37 blade, the same type of contact initiation is used. An external monoharmonic forcing is applied on the first bending mode shape $\mathbf{\Phi}_{1B}$ with a varying amplitude A, such as

$$\mathbf{f}_{ex}(t) = A\mathbf{M}\mathbf{\Phi}_{1B}\cos(\omega t) \tag{31}$$

and the obstacle is a circular rigid casing, depicted in Fig. 23. Since the casing is rigid, the relative displacement condensation presented in section A.2 is not applicable since time-invariant node-to-node contact pairs cannot be formed.

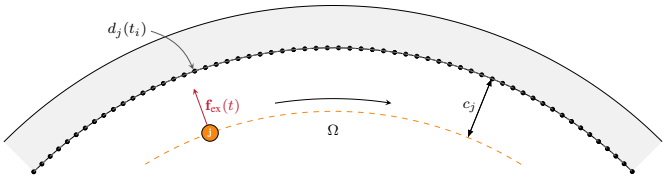

Figure 23. Circular rigid casing.

The initial gap between each boundary node and the casing is the same for all nodes and is set to $c_j = 4 \cdot 10^{-4}\,\mathrm{m}$. In order not to introduce nonlinear nonconservative effects in the Melnikov analysis, friction is neglected. This hypothesis strongly affects the physical nature of the contact interactions, however for this application the main concern is to apply the isola detection procedure to industrial models featuring multiple nonlinear nodes. The extension to nonconservative nonlinearities requires a modification of the Melnikov function by introducing the nonlinear dissipative terms. Such modifications were made in very recent works on a low-dimensional parametric oscillator featuring dry friction [19]. For the sake of brevity, the modification of the Melnikov function for rubbing interactions on industrial models will be dealt with in future work.

4.3 Complex nonlinear normal modes

The dynamics of industrial models are usually strongly influenced by the structural damping rates, this is why it is important to use dedicated strategies for the computation of nonlinear normal modes allowing to account for damping effects. By doing so, the solutions composing the nonlinear normal modes are closer to the actual nonlinear resonances obtained in forced-response. It was observed that the continuation of conservative nonlinear modes on the blade model suffered from the presence of singular points, similarly as on the academic application. Indeed, a large number of singular points exist on industrial applications because of the modal density of such models: each intersection of their eigenfrequencies with an engine order (harmonic) yields a singular point. However, all these intersections are not observed in forced response because they are damped out by the structural damping. Hence,

taking structural damping into account in the nonlinear modes allows to filter out the singular points that play no role in forced response. This behavior does not apply on the academic model: singular points persist even when accounting for damping, so conservative modes were kept in section 3.

In order to take structural damping into account in the computation of NNM, the complex nonlinear normal mode strategy is retained [56, 70, 91]. This formalism is presented in C.

When applying Melnikov's energy principle, the nonlinear damping ζ is not used to compute the work and dissipated energy. The introduction of ζ, accounting for structural damping, is made to compute nonlinear mode shapes which phasing are adjusted by accounting for damping. Thus, the value of the integral $\mathcal{R}(\mathbf{C})$ (Eq. (20)) is more coherent with what is actually dissipated in a time period by damping. Mode shapes are then considered to be perfectly periodic and they only differ from conservative mode shapes because their phasing is modified by the introduction of structural damping by means of ζ.

4.4 Melnikov analyses and isola detection

The isola detection strategy is carried out in this section and the steps presented in section 2.6 are followed. Firstly, a nonlinear modal analysis is performed in section 4.4.1. In the sections 4.4.2 and 4.4.3 Melnikov analyses are carried out to detect isolas and prove the applicability of the strategy to industrial models. The relevance of isolated branches is assessed through time integration simulations in section 4.4.4. Finally, an overview of the dynamics of the system is given in section 4.4.5. For this study, $N_\mathrm{h} = 10$ harmonics are retained and $\varepsilon = 1 \cdot 10^7\,\mathrm{N{\cdot}m^{-1}}$ is used.

4.4.1 Nonlinear modal analysis

In order to perform Melnikov analyses, the computation of a conservative NNM is required. However, for the case of industrial systems it is necessary to account for the structural damping in order to obtain representative NNM. For this reason, Melnikov analyses on rotor 37 are carried out with a complex NNM even though it is outside of the initial theoretical scope proposed by Cenedese and Haller [18]. Some work was also carried out on the energy balance method [50, 51] to use the extended periodic motion concept (EPMC) [73], an other type of damped NNM. The impact of using complex NNM is addressed in the sections 4.4.2 and 4.4.3 in the light of the results obtained. The effect of using damped nonlinear modes is also mitigated by the fact that a slow exponential decay hypothesis (*i.e.* $\zeta \ll \omega$) is made for the setup of complex nonlinear modes. Indeed, solutions belonging to damped NNM thus remain *almost* periodic, allowing to process them through Melnikov analyses.

By applying the damped nonlinear modal analysis presented in section 4.3, a single NNM is obtained in this configuration and displayed in Fig. 24 alongside a NFRC for $A = 1{,}500$. The fact that only one NNM is responsible for the nonlinear dynamics of the system makes the Melnikov analyses simpler as no preamble exhaustive research of all NNM through multiple types of initializations is needed.

4.4.2 Coexisting isolated branches

By carrying out a Melnikov analysis for $A = 550$, three isolated branches are predicted, the full view of the nonlinear response of the blade for this level of forcing is depicted in Fig. 25.

It is observed by increasing A that the different isolated branches merge with the main NFRC similarly as in section 3.4. Consequently, isolas are colored in Fig. 25 to associate them with their merge threshold value of A. Isola 1 is identified in red (—) because it is associated with a merge around $A = 625$. Isolas 2 and 3 are colored in blue (—) and are merging with the main NFRC around $A = 2{,}650$. Both isolated branches of solutions merge with the main curve around the same value $A = 675$, this behavior is explored in section 4.4.3.

The three isolated branches identified in Fig. 25 are very critical from a design viewpoint: all three are of higher amplitudes than the main NFRC's nonlinear resonance. For instance the maximum amplitude for isola 3 is four times higher than the main nonlinear resonance's amplitude. All isolated branches also feature high frequency shifts from the main nonlinear resonance which makes their research arduous without proper methodological tools. This is why isolated branches should be systematically searched for by dedicated strategies such as the Melnikov analysis as a way to ensure that industrial design criteria are met on an exhaustive nonlinear dynamics response containing all eventual isolated branches, and not only the main NFRC.

Two critical areas on the NNM are identified to be responsible of the disconnection of the isolated branches with the main curve, the first one (i) is around $\omega = 6{,}200\,\mathrm{rad{\cdot}s^{-1}}$ and the second one (ii) around $\omega = 6{,}550\,\mathrm{rad{\cdot}s^{-1}}$. In

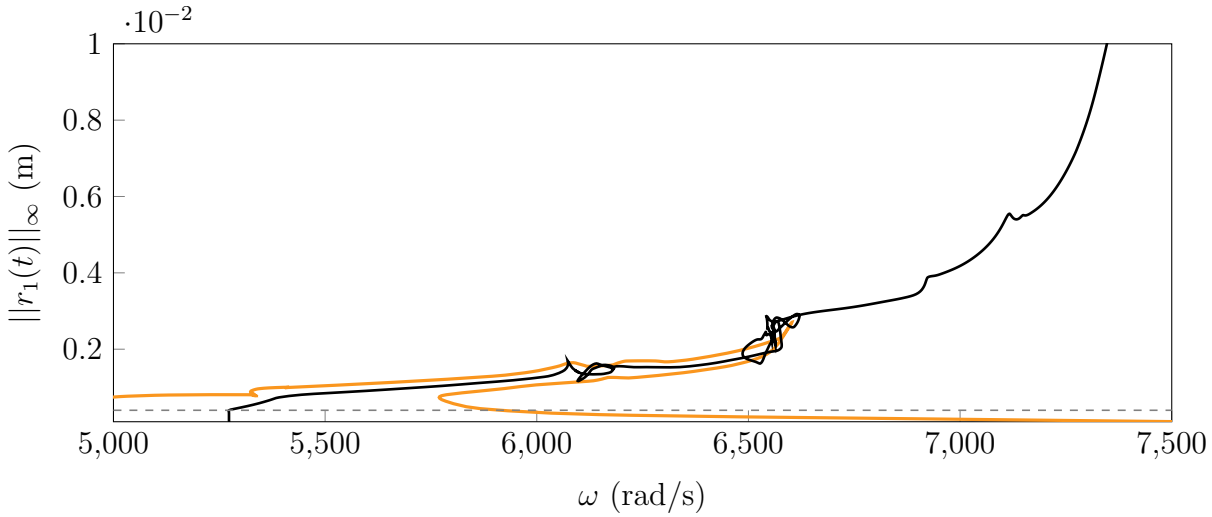

Figure 24. Complex nonlinear mode associated to the first bending mode of rotor 37 (—), NFRC for $A = 1{,}500$ (—), c_1 (- -).

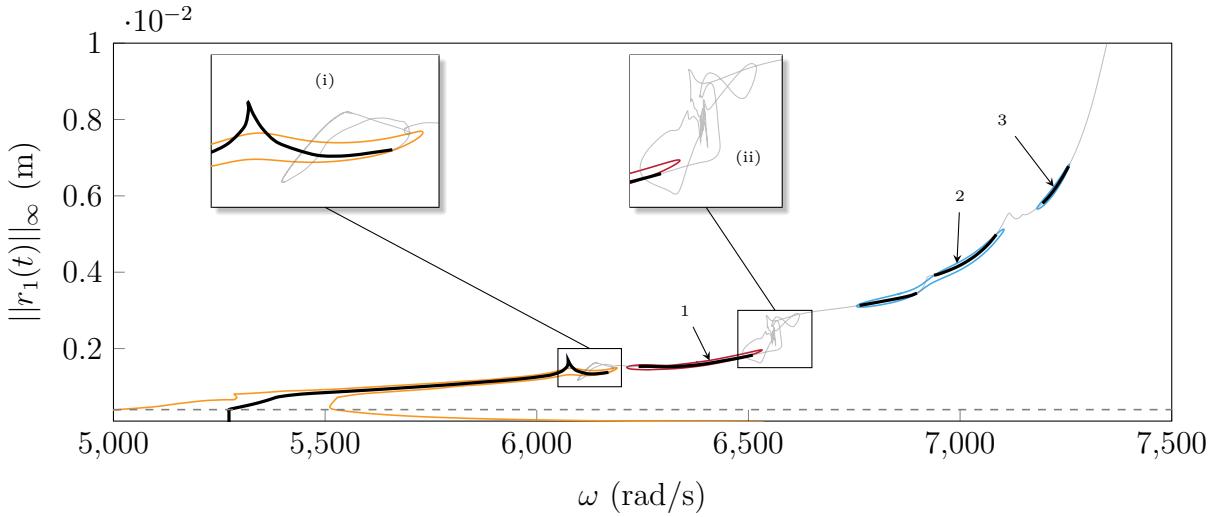

Figure 25. Result of the Melnikov analysis for $A = 550$, NNM (—), NFRC (—), isolated branches (—) (—), two periodic orbits persist ($\overline{\mathcal{M}}^{1:1} > 0$) (—), no periodic orbits persist ($\overline{\mathcal{M}}^{1:1} < 0$) (—), c_1 (- -).

these areas, the NNM experiences sudden gains of amplitude before looping and pursuing the locus of nonlinear resonances. The reasons behind the separation of isolated branches are attributed to these sudden gains in amplitude in the response amplitude/pulsation plane. Indeed, these come with higher velocities and thus higher dissipated energies by the structural damping. This phenomenon is also identified in section 3.4.2 for the second family of isolated branches on the phenomenological model. Damping effects appear to be central since the resistance term $\mathcal{R}$—quantifying the dissipated energy over one period—influences the amount of energy needed so that solutions of the NNM persist in forced response. When the resistance locally rises, it creates a barrier of energy preventing the existence of solutions connected to the rest of the NFRC. On the contrary, when the resistance locally diminishes, it allows the existence of isolated solutions by forming a energy well. For the NNM of rotor 37, the resistance term is depicted in Fig. 26 alongside with the work of the forcing term for $A = 550$. The resistance is invariant with the level of forcing as it only depends on the dissipated energy by structural damping.

Melnikov's criterion states that solutions persist from the NNM for this level of forcing when the work of forcing

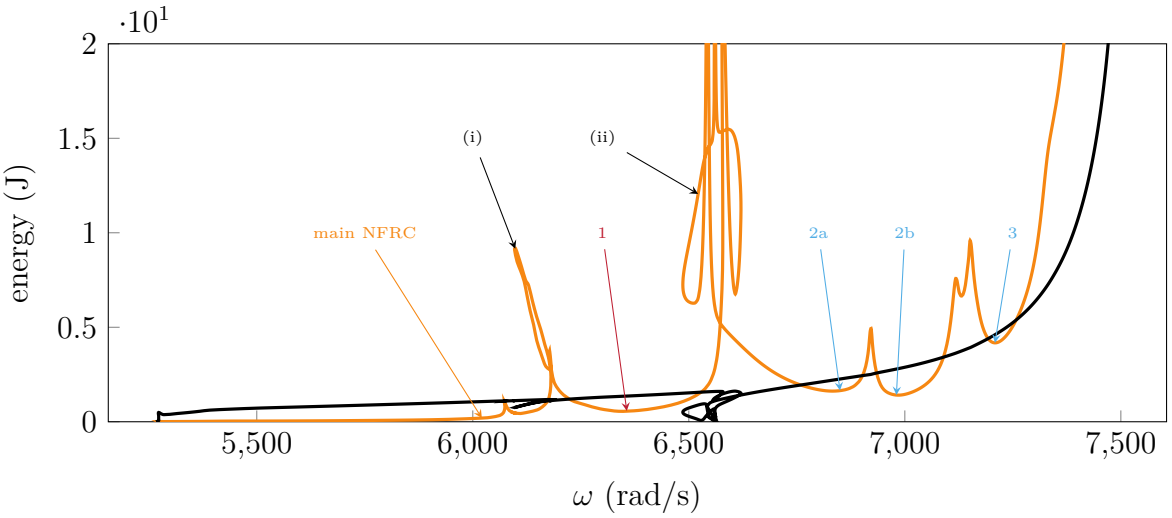

Figure 26. View of the energy balance for $A = 550$, work of the forcing term $\left|W^{1:1}\right|$ (—), resistance $|\mathcal{R}|$ (—).

term $\left|W^{1:1}\right|$ (—) is higher than the resistance $|\mathcal{R}|$ (—), *i.e.* $\overline{\mathcal{M}}^{1:1} = \left|W^{1:1}\right| - |\mathcal{R}| > 0$. Several wells of energy are easily identified in Fig. 26, they are delimited with local peaks of resistance preventing the solutions from being connected with the main NFRC at lower frequencies. In the following, these peaks are designated by the term barrier of energy. The local minima of these wells of energy are the loci of apparition of isolated branches: four local minima are identified to be responsible of the appearance of four isolas. Minima 2a and 2b on Fig. 26 are associated with the same number since a single isola covering the whole frequency range of the two wells is observed at $A = 550$, see Fig. 25. Isola 2 is in fact the result of a merger between two different isolated branches at lower forcing amplitudes. In this case, the examination of the NNM in terms of energy provides valuable information about the existence of specific regions susceptible to give birth to isolated solutions.

The physical mechanisms behind the appearance of the peaks of resistance are investigated by examining the relative modal contributions $||\gamma_j(t)||_{\infty,\text{rel}}$ along the NNM. The relative modal contributions are computed for each mode, say the j-th, such as

$$||\gamma_j(t)||_{\infty,\text{rel}} = \frac{\max\limits_{i\in[\![1,N_t]\!]} |\gamma_j(t_i)|}{\sum\limits_{k=1}^{n} \max\limits_{i\in[\![1,N_t]\!]} |\gamma_k(t_i)|}. \tag{32}$$

The examination of these quantities provides information about the global dynamics of the blade for each solution. For a given solution, the relative modal contributions sum up to one allowing to observe relative evolutions of each mode along a family of solutions. The $n = 34$ relative modal contributions along the NNM are depicted in Fig. 27.

The strong contribution of the 1B mode along the whole mode, and especially at low frequencies, accounts for the fact that the NNM is associated with the first bending mode. This contribution diminishes as the frequency—and the response amplitude—increases because of the nonlinear nature of the mode. Both barriers of energy (i) and (ii), initially identified in Fig. 26, are also found in Fig. 27 in the form of sudden decreases of the relative modal contribution of the 1B mode. For the first barrier (i), a low decrease of the relative modal contribution of the 1B mode and a simultaneous rise of the relative modal contribution of the fifth mode is observed. For the second barrier (ii), a much more complex behavior is exhibited, but the same observations can be made. A strong decrease of the 1B mode contribution is detected and a significant rise of the contributions of both the 2B mode and the seventh mode (associated with $\omega_7 = 51{,}926.6\,\text{rad}\cdot\text{s}^{-1}$). Both barriers (i) and (ii) are also close to fractions of the linear eigenfrequencies of the modes that suddenly raise ($\frac{\omega_5}{6}$ for (i), $\frac{\omega_{2B}}{3}$ and $\frac{\omega_7}{8}$ for (ii)). These fractions are underestimating the actual frequencies where the decreases of 1B modal contribution happen because the linear

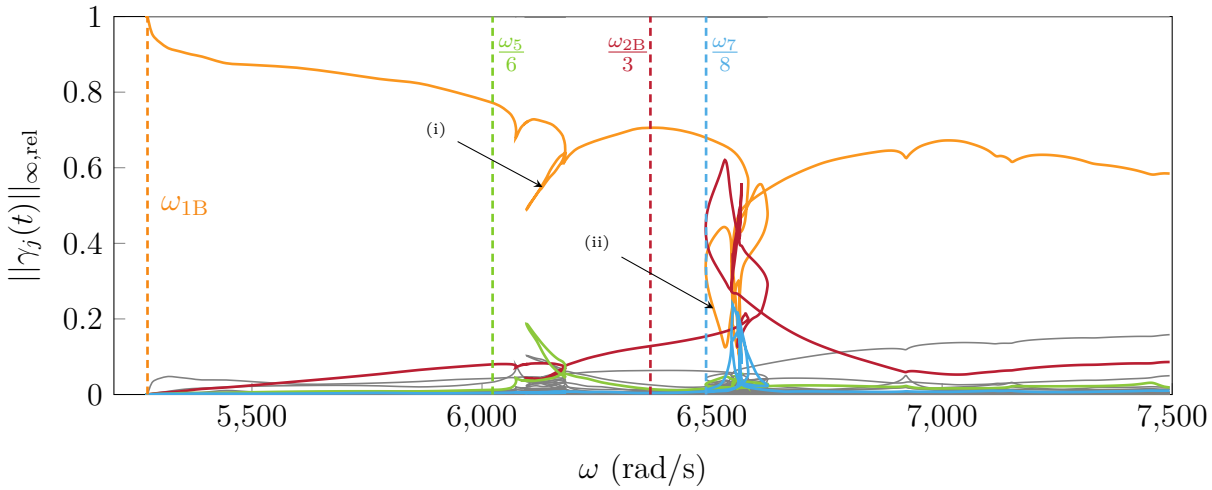

Figure 27. Relative modal contributions on the NNM, 1B mode (—), mode 3 (—), mode 5 (—), mode 7 (—), other modes (—).

eigenfrequencies are used. Indeed, the actual eigenfrequencies are most likely shifted towards higher frequencies due to nonlinear effects.

The observations made on barriers (i) and (ii) support the idea that the barriers of energy in the resistance are associated with nonlinear modal interactions. The fact that nonlinear resonances can be isolated from the main NFRC because of nonlinear modal interactions was already suggested in the literature [13, 15] for smooth nonlinearities. The results given by the quantitative analysis of the resistance curve in the present work is consistent with this affirmation.

4.4.3 Isola merging

An interesting behavior is captured on the isolas 2 and 3 represented in Fig. 25: the two isolas experience a merger at a threshold value of around $A = 675$. A Melnikov analysis for $A = 700$ is depicted in Fig. 28 and the isolas 2 and 3 are also represented in gray (—) for $A = 650$ in order to highlight this merger.

At this forcing amplitude value $A = 700$, the isola 1 (—) is now merged with the main NFRC, however the Melnikov function predicts that both sides are still disjoint. This effect, already observed in sections 3 and 4.4.2, can be attributed to the fact that Melnikov analyses are based on a first order Taylor expansion that can be ill-suited for sensitive regions such as close to a merger between two branches of solutions. The same exact observation is made at the merger of isolas 2 and 3. The Melnikov analysis predicts that no solutions persist between the two sides in the zoomed frame, whereas the arc-length continuation shows that it forms a single branch. In the case of rotor 37, this effect can also be attributed to the violation of the conservative NNM hypothesis since damped NNM are used to perform the Melnikov analyses. However, an excellent agreement is still observed between the areas where Melnikov analyses predict the persistence of solutions and the actual presence of solutions.

4.4.4 Validation of isolated solutions with time marching simulations

Time marching simulations are run in order to assess the relevance of the different isolated branches of periodic solutions captured through HBM. An industrial state-of-the-art strategy [29] relying on Lagrange multipliers is applied in order to produce these reference simulations. Numerous initial conditions from the HBM branches are given to the time integrator. These initial conditions are then integrated over four hundred periods with a time step of $h = 1 \cdot 10^{-7}$ s and the corresponding amplitudes of response (o) are displayed in Fig. 29 for the radial displacement at the leading edge. A strong correlation is observed between the branches of periodic solutions computed by HBM and the corresponding TI solutions. Only few solutions do not remain on the same periodic orbits. By providing HBM initial conditions to the time integrator, a perturbation is applied to the periodic orbits. This perturbation

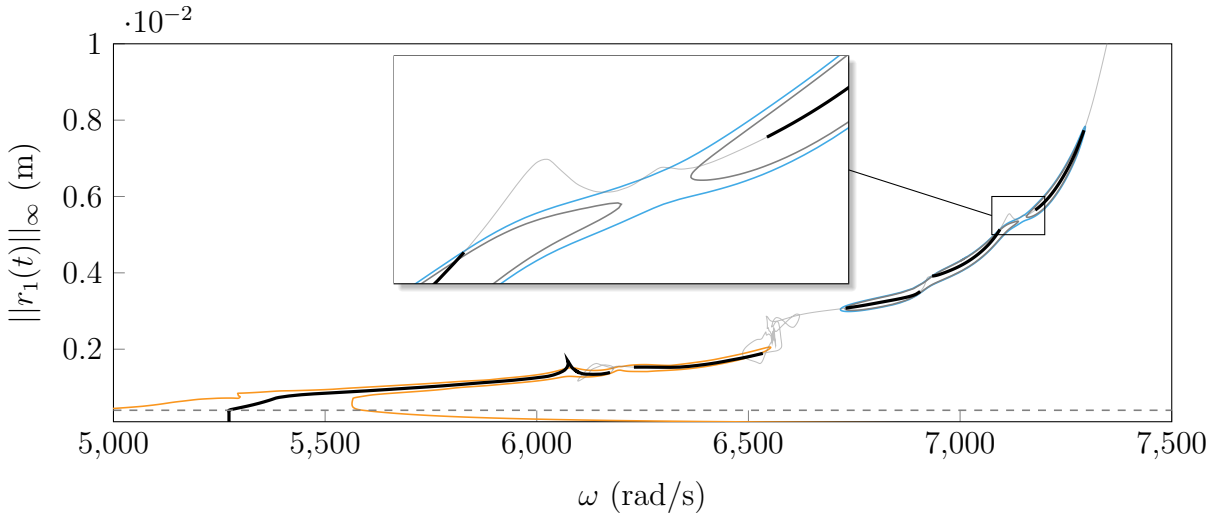

Figure 28. Result of the Melnikov analysis for $A = 700$, NNM (—), NFRC $A = 700$ (—), isolated branch $A = 700$ (—), isolated branches $A = 650$ (—), two periodic orbits persist ($\overline{\mathcal{M}}^{1:1} > 0$) (—), no periodic orbits persist ($\overline{\mathcal{M}}^{1:1} < 0$) (—), c_1 (- -).

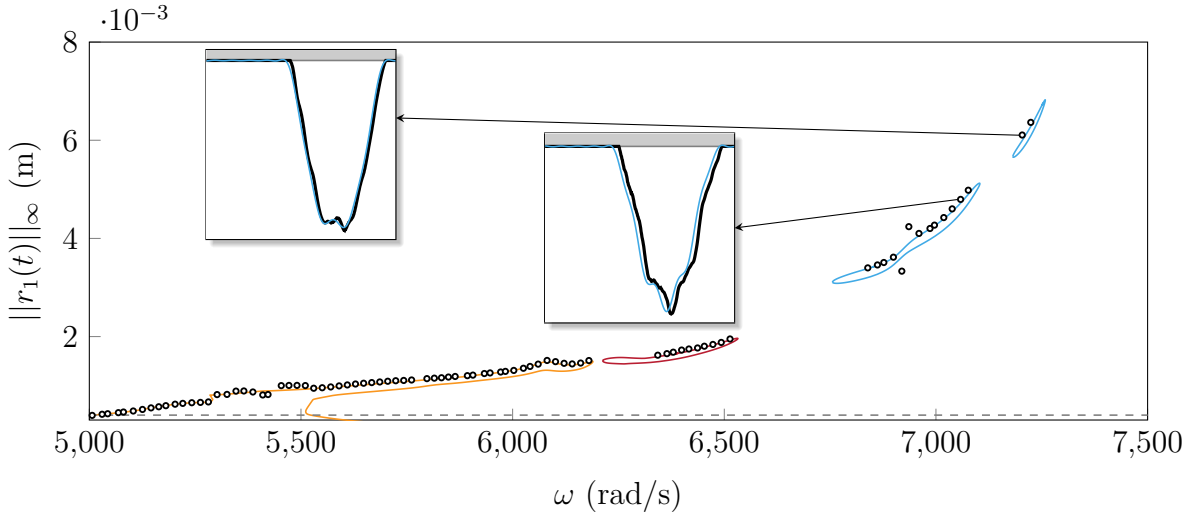

Figure 29. Correlation of time marching simulations with DLFT-HBM for $A = 550$, NFRC (—), isolated branches (—) (—), TI solutions (o), c_1 (- -). Displacement graphs for $r_1(t)$: DLFT-HBM (—), TI (—), casing (▭).

lies mainly in the difference in terms of contact treatment and in terms of representation of the solutions (Fourier series for HBM and time-discrete for TI). If TI solutions remain on the same orbit as HBM solutions, then this perturbation has vanished. It reflects a certain level of local stability of these periodic orbits. Since very remote solutions on isolated branches are captured through TI in Fig. 29, the research of isolated branches in nonlinear studies is crucial. Typical continuation techniques miss such solutions even though they can have detrimental effects on the lifespan and the safety of the system.

For the same reasons given in section 3.5, a dedicated local stability analysis exceeds the scope of this paper and is thus not conducted.

4.4.5 Prediction of nonlinear resonances

The accuracy of Melnikov analyses can be used to predict the locus of nonlinear resonances at a very low computational effort for several values of A, whether they belong to an isolated branch or to the main NFRC. The prediction of the locus of nonlinear resonances by Melnikov analyses (●) is compared to the actual nonlinear resonances measured on the main NFRC (●) at different amplitudes. Melnikov analyses also allowed to compute the isolated branches and the associated resonances (●) (●). All four categories are depicted in Fig. 30.

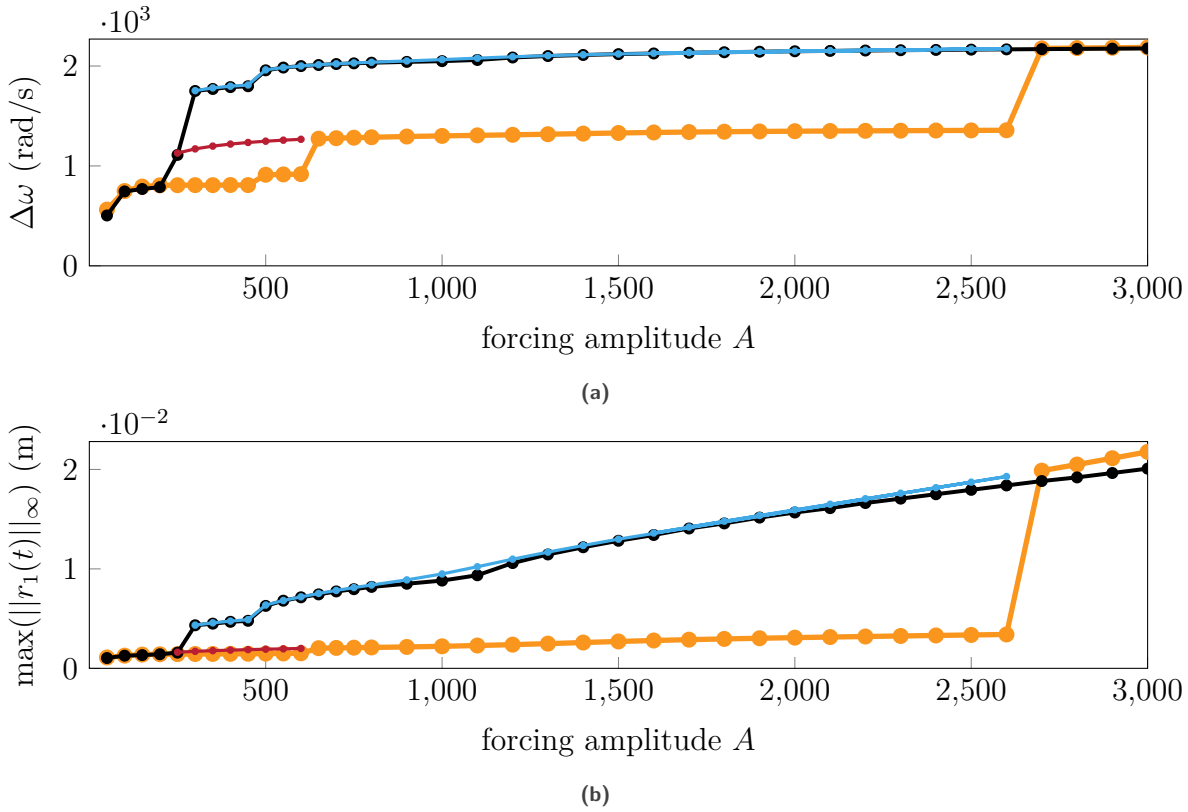

Figure 30. Evolution of the nonlinear resonances with A for rotor 37, (a) stiffening effect, (b) maximum displacement, main NFRC (●), prediction by Melnikov analyses (●), isola family 1 (●), isola family 2 (●).

The supplementary information given by Melnikov analyses on the locus of nonlinear resonances allows to observe both the actual maximum response amplitude and stiffening effect (computed with respect to the 1B mode). Both Melnikov and NFRC measurements are in agreement at very low and very high forcing amplitudes since no isolated branches exist in these areas. Nevertheless, in between these areas, both response amplitudes and stiffening effects are highly underestimated by classical continuation techniques. It underlines that the classical NFRC calculations give a partial view of the real dynamics response of the system.

The Melnikov predictions (●) are still featuring discontinuous behaviors, these discontinuities are associated with the birth of isolated branches (●) (●). They appear along the NNM remotely from the previous nonlinear resonance, near the wells of energy identified in section 4.4.2.

As in section 3.4.4, the Melnikov analyses predictions are in excellent agreement with the maximum amplitude captured on the computed isolated branches. The computation of the isolated branches is then not necessary if the only information sought is the maximum response amplitude and the associated stiffening effect.

5 Conclusion

This paper addresses the research of isolated branches of solutions associated to nonlinear normal modes in a forced response configuration for a system with contact interfaces. An isola detection procedure is proposed by combining complex non linear modes with Melnikov's energy principle. This procedure is carried out on a phenomenological model to demonstrate its accuracy on a numerically challenging example. The applicability of the procedure is also proven on an industrial rotor compressor blade model, making it suitable for the detection of isolated branches in complex configurations. The proposed procedure is relatively light computationally wise, since it relies on the computation of an energy balance on the solutions of a nonlinear normal mode.

Discontinuous behaviors are observed with respect to the level of forcing in the forced response configuration. A large number of nonlinear normal modes are uncovered for the phenomenological model, demonstrating that the intricate dynamics of the system is driven by multiple nonlinear modes. The use of the isola detection procedure allows the detection of several families of isolated branches whose mergers with the NFRC are responsible for the discontinuities. These families of isolated branches are observed to be systematically of higher response amplitude and more frequentially shifted than the nonlinear resonances of the main NFRC, making the research of isolated branches crucial when accounting with nonlinear dynamics of a system in a forced response configuration. The different isolated branches are shown to contain at least locally stable solutions by carrying out time integration computations.

The isola detection procedure is then applied to an industrial blade model on which the same NFRC discontinuities phenomena are observed. An adjustment of the procedure is needed in order to carry out the isola detection: complex nonlinear normal modes are used to account for structural damping. Such damped modes are outside the scope of the initial Melnikov analyses [18], however it is shown in this work that the presence of isolas is still very accurately predicted by the procedure. By analyzing the different terms in the energy balance function, some clues are given regarding the fact that the existence of isolated branches is closely related to barriers and wells of energy in the resistance term of the Melnikov analysis. The analysis of the nonlinear normal mode is supporting the idea that nonlinear modal interactions are responsible of the existence of such barriers of energy. The analysis of nonlinear normal modes in the light of the energy principle also allows to identify in advance the susceptible loci for the birth of isolas. Mergers between isolated branches are also observed but remain not precisely predicted by Melnikov analyses. This defect is most likely associated with the first order Taylor expansion used in the derivation of the Melnikov function that is not accurate enough in sensitive areas. Finally, Melnikov analyses lead to an accurate estimate of the location of nonlinear resonances with respect to the forcing amplitude, that is highly underestimated by classical continuation techniques when isolated branches exist.

The applicability and accuracy of an inexpensive isola detection strategy is demonstrated in this paper on a highly challenging industrial application. It opens up perspectives on the research of isolated branches for a wide variety of industrial systems featuring nonlinearities. Future works must address the extension of the Melnikov analysis to industrial nonconservative systems featuring dry friction, as it was already done on a low-dimensional phenomenological model [19]. The emergence of a methodology to tackle high-dimensional systems featuring non conservative nonlinearities would be highly beneficial for the study of systems featuring dry friction for instance for which isolated branches were already observed [6]. As a way of contributing to lift the difficulty to highlight isolated branches of solutions on industrial systems, the procedure proposed in this article systematically identifies isolated branches of periodic solutions associated to nonlinear normal modes, allowing to have a more exhaustive view of the dynamics response of all nonlinear industrial systems.

Acknowledgments

This research was undertaken thanks to funding from the Canada Research Chairs Program.

A Condensation of the frequency-domain problem

Both condensation procedures presented in this appendix were extracted from the literature [63]. The first one (A.1) is used to condense linear degrees of freedom and the second one (A.2) is tailored for time-invariant node-to-node contact interactions that condense nonlinear dof as relative displacements.

A.1 Condensation of linear degrees of freedom

The harmonic equation of motion (5) contains $n(2N_\mathrm{h}+1)$ unknowns standing for the real Fourier coefficient of each dof. In the case of localized nonlinearities, *i.e.* not every dof is subject to nonlinear forces, it is possible to reduce the size of the problem without making any approximation on the solutions of the problem. The size of the system then becomes $n_\mathrm{nl}(2N_\mathrm{h}+1)$ with n_nl the number of dof that withstand nonlinear forces. This type of condensation is possible thanks to the algebraic nature of the harmonic system. In order to perform the condensation, the dof of the system should be partitioned according to their nature, linear dof $\widetilde{\mathbf{x}}_\mathrm{L}$ and nonlinear ones $\widetilde{\mathbf{x}}_\mathrm{nl}$. For the sake of clarity, the partitioned system is also reorganized so that the unknown vector reads $\widetilde{\mathbf{x}} = \begin{bmatrix}\widetilde{\mathbf{x}}_\mathrm{L} & \widetilde{\mathbf{x}}_\mathrm{nl}\end{bmatrix}^\top$ and it yields

$$\begin{bmatrix}\mathbf{Z}_{\mathrm{L,L}} & \mathbf{Z}_{\mathrm{L,nl}} \\ \mathbf{Z}_{\mathrm{nl,L}} & \mathbf{Z}_{\mathrm{nl,nl}}\end{bmatrix}\begin{bmatrix}\widetilde{\mathbf{x}}_\mathrm{L} \\ \widetilde{\mathbf{x}}_\mathrm{nl}\end{bmatrix} + \begin{bmatrix}\mathbf{0} \\ \widetilde{\mathbf{f}}_\mathrm{nl,nl}\end{bmatrix} = \begin{bmatrix}\widetilde{\mathbf{f}}_\mathrm{ex,L} \\ \widetilde{\mathbf{f}}_\mathrm{ex,nl}\end{bmatrix}. \tag{33}$$

Expressing $\widetilde{\mathbf{x}}_\mathrm{L}$ with respect to $\widetilde{\mathbf{x}}_\mathrm{nl}$ yields

$$\widetilde{\mathbf{x}}_\mathrm{L} = \mathbf{Z}_{\mathrm{L,L}}^{-1}\left(\widetilde{\mathbf{f}}_\mathrm{ex,L} - \mathbf{Z}_{\mathrm{L,nl}}\widetilde{\mathbf{x}}_\mathrm{nl}\right), \tag{34}$$

and finally, by substituting $\widetilde{\mathbf{x}}_\mathrm{L}$ into Eq. (33), one obtains the condensed system

$$\mathcal{H}_\mathrm{red}(\widetilde{\mathbf{x}}_\mathrm{red},\omega) = \mathbf{Z}_\mathrm{red}\widetilde{\mathbf{x}}_\mathrm{nl} + \widetilde{\mathbf{f}}_\mathrm{nl,red} - \widetilde{\mathbf{f}}_\mathrm{ex,red} = \mathbf{0} \tag{35}$$

where

$$\mathbf{Z}_\mathrm{red} = \mathbf{Z}_{\mathrm{nl,nl}} - \mathbf{Z}_{\mathrm{nl,L}}\mathbf{Z}_{\mathrm{L,L}}^{-1}\mathbf{Z}_{\mathrm{L,nl}}, \tag{36}$$

$$\widetilde{\mathbf{f}}_\mathrm{ex,red} = \widetilde{\mathbf{f}}_\mathrm{ex,nl} - \mathbf{Z}_{\mathrm{nl,L}}\mathbf{Z}_{\mathrm{L,L}}^{-1}\widetilde{\mathbf{f}}_\mathrm{ex,L} \tag{37}$$

and

$$\widetilde{\mathbf{f}}_\mathrm{nl,red} = \widetilde{\mathbf{f}}_\mathrm{nl,nl}. \tag{38}$$

A.2 Condensation of nonlinear degrees of freedom

In the case of two contacting structures, one may formulate the contact constraints thanks to the gap function g (or relative displacement x_r). For a system involving a single contact constraint, the gap function reads

$$g(t) = x^1(t) - x^2(t) + g_0 \tag{39}$$

where $x^1(t)$ and $x^2(t)$ respectively refer to the nonlinear dof of each of the two contacting structures. g_0 is the initial gap between the contact nodes of both structures. This configuration is illustrated for 1D structures in Fig. 31.

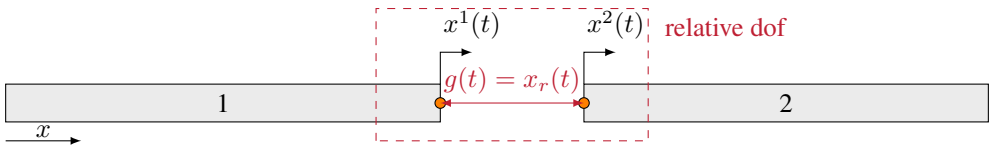

Figure 31. Relative dof formalism in 1D.

Since nonlinear contact forces depend on relative quantities and are reciprocal, the harmonic equation of motion can be formulated in terms of relative displacements $\mathbf{x}_\mathrm{r}(t)$. It yields a reduction of the total size of the system by a

factor two, making its condensed size $\frac{n_{\mathrm{nl}}}{2}(2N_{\mathrm{h}}+1)$. In order to perform this condensation, one should express the harmonic equation of motion for both structures, respectively identified by superscripts 1 and 2 such as

$$\begin{cases} \mathbf{Z}^1_{\mathrm{red}}\widetilde{\mathbf{x}}^1_{\mathrm{nl}} + \widetilde{\mathbf{f}}^1_{\mathrm{nl,red}}\left(\widetilde{\mathbf{x}}^1_{\mathrm{nl}}, \widetilde{\mathbf{x}}^2_{\mathrm{nl}}\right) = \widetilde{\mathbf{f}}^1_{\mathrm{ex,red}} & \text{(40a)} \\ \mathbf{Z}^2_{\mathrm{red}}\widetilde{\mathbf{x}}^2_{\mathrm{nl}} + \widetilde{\mathbf{f}}^2_{\mathrm{nl,red}}\left(\widetilde{\mathbf{x}}^1_{\mathrm{nl}}, \widetilde{\mathbf{x}}^2_{\mathrm{nl}}\right) = \widetilde{\mathbf{f}}^2_{\mathrm{ex,red}}. & \text{(40b)} \end{cases}$$

The reciprocity of contact forces reads

$$\widetilde{\mathbf{f}}^1_{\mathrm{nl,red}}\left(\widetilde{\mathbf{x}}^1_{\mathrm{nl}}, \widetilde{\mathbf{x}}^2_{\mathrm{nl}}\right) = -\widetilde{\mathbf{f}}^2_{\mathrm{nl,red}}\left(\widetilde{\mathbf{x}}^1_{\mathrm{nl}}, \widetilde{\mathbf{x}}^2_{\mathrm{nl}}\right) = \widetilde{\mathbf{f}}_{\mathrm{nl,r}}. \tag{41}$$

In order to make the relative displacement $\widetilde{\mathbf{x}}_{\mathrm{r}} = \widetilde{\mathbf{x}}^1_{\mathrm{nl}} - \widetilde{\mathbf{x}}^2_{\mathrm{nl}}$ appear, one has to multiply Eq. (40a) by $\left(\mathbf{Z}^1_{\mathrm{red}}\right)^{-1}$, Eq. (40b) by $\left(\mathbf{Z}^2_{\mathrm{red}}\right)^{-1}$, use the reciprocity relation (41) and subtract Eq. (40b) to Eq. (40a), yielding

$$\widetilde{\mathbf{x}}^1_{\mathrm{nl}} - \widetilde{\mathbf{x}}^2_{\mathrm{nl}} + \left(\left(\mathbf{Z}^1_{\mathrm{red}}\right)^{-1} + \left(\mathbf{Z}^2_{\mathrm{red}}\right)^{-1}\right)\widetilde{\mathbf{f}}_{\mathrm{nl,r}} = \left(\mathbf{Z}^1_{\mathrm{red}}\right)^{-1}\widetilde{\mathbf{f}}^1_{\mathrm{ex,red}} - \left(\mathbf{Z}^2_{\mathrm{red}}\right)^{-1}\widetilde{\mathbf{f}}^2_{\mathrm{ex,red}}. \tag{42}$$

Equation (42) is then multiplied by $\mathbf{Z}_{\mathrm{r}} = \left(\left(\mathbf{Z}^1_{\mathrm{red}}\right)^{-1} + \left(\mathbf{Z}^2_{\mathrm{red}}\right)^{-1}\right)^{-1}$ in order to retrieve the classical form of the harmonic equation of motion

$$\mathbf{Z}_{\mathrm{r}}\left(\widetilde{\mathbf{x}}^1_{\mathrm{nl}} - \widetilde{\mathbf{x}}^2_{\mathrm{nl}}\right) + \widetilde{\mathbf{f}}_{\mathrm{nl,r}} = \mathbf{Z}_{\mathrm{r}}\left(\left(\mathbf{Z}^1_{\mathrm{red}}\right)^{-1}\widetilde{\mathbf{f}}^1_{\mathrm{ex,red}} - \left(\mathbf{Z}^2_{\mathrm{red}}\right)^{-1}\widetilde{\mathbf{f}}^2_{\mathrm{ex,red}}\right). \tag{43}$$

Finally, the condensed external forces $\widetilde{\mathbf{f}}_{\mathrm{ex,r}}$ can be identified such as

$$\widetilde{\mathbf{f}}_{\mathrm{ex,r}} = \mathbf{Z}_{\mathrm{r}}\left(\left(\mathbf{Z}^1_{\mathrm{red}}\right)^{-1}\widetilde{\mathbf{f}}^1_{\mathrm{ex,red}} - \left(\mathbf{Z}^2_{\mathrm{red}}\right)^{-1}\widetilde{\mathbf{f}}^2_{\mathrm{ex,red}}\right). \tag{44}$$

The resulting condensed equation of motion in the frequency domain reads

$$\mathcal{H}_{\mathrm{r}}(\widetilde{\mathbf{x}}_{\mathrm{r}}, \omega) = \mathbf{Z}_{\mathrm{r}}(\omega)\widetilde{\mathbf{x}}_{\mathrm{r}} + \widetilde{\mathbf{f}}_{\mathrm{nl,r}} - \widetilde{\mathbf{f}}_{\mathrm{ex,r}} = \mathbf{0}. \tag{45}$$

Both condensations of linear dof (A.1) and nonlinear dof (A.2) are exact condensation procedures, thus not modifying the solutions of the problem. However, since the procedures involve matrix inversions, the numerical quality and conditioning of the problem should be carefully monitored.

B Validation of numerical parameters simulations

Reference simulations are run in order to confirm that the numerical parameters used for the HBM are suitable to consider that the solutions are converged in terms of dynamics. A first NFRC computed for the forcing amplitude $A = 1$ is depicted in Fig. 32. Time signals at the nonlinear resonance obtained through DLFT-HBM are also displayed in Fig. 33 and superimposed with their time integration (TI) counterpart. In order to compute the TI solution at the resonance, initial conditions obtained by DLFT-HBM are provided to the time integrator. These initial conditions are integrated over 100 periods so that the steady-state is reached.

It is observed in Fig. 33 that the response computed through HBM at the nonlinear resonance is converged with respect to the solution obtained through TI in terms of displacement, velocity and contact force. This excellent agreement allows to conclude that the numerical parameters chosen for the HBM are well-suited for the presented study.

C Complex nonlinear mode formalism

The formalism of complex nonlinear modes is presented in this appendix, it allows to find free solutions to the nonconservative normalized equation of motion

$$\frac{\alpha}{\beta^2}\mathbf{M}\ddot{\mathbf{x}}(t) + \frac{\alpha}{\beta}\mathbf{C}\dot{\mathbf{x}}(t) + \alpha\mathbf{K}\mathbf{x}(t) + \mathbf{f}_{\mathrm{nl}}(\mathbf{x}(t), \dot{\mathbf{x}}(t)) = \mathbf{0}. \tag{46}$$

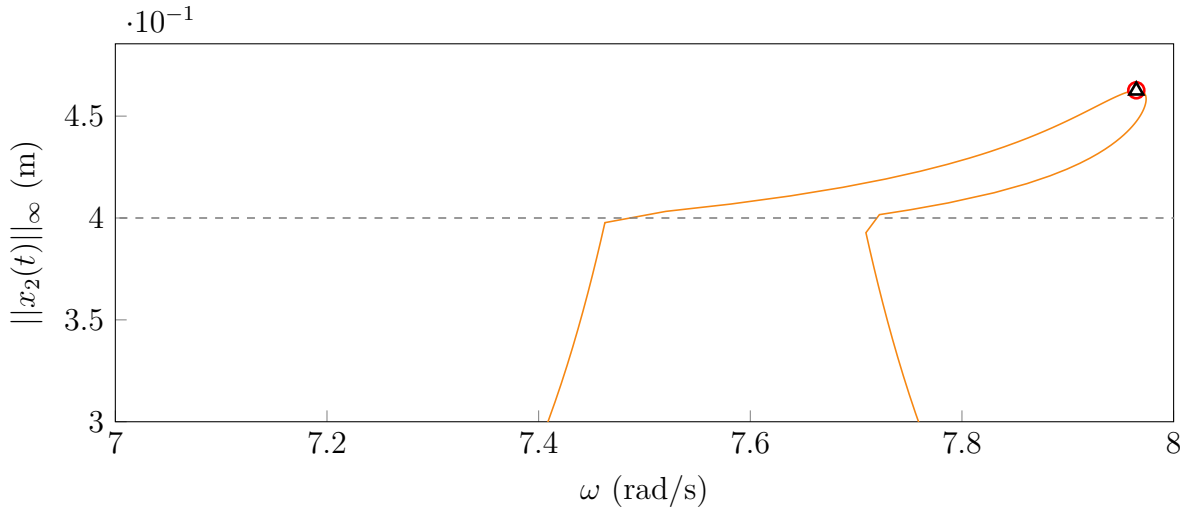

Figure 32. NFRC with $A = 1$ (—), g_0 (- -), DLFT-HBM solution at resonance (●), TI solution at resonance (▲).

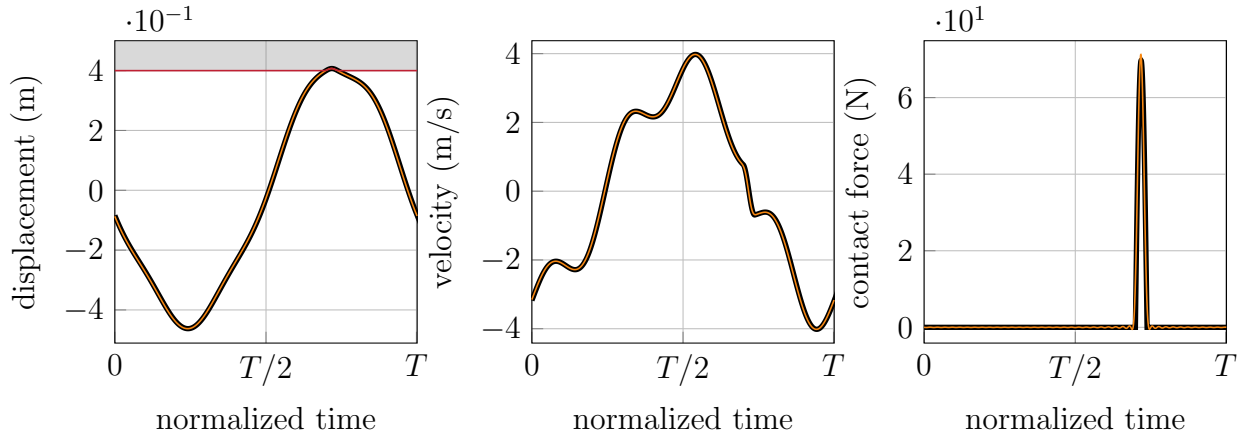

Figure 33. Solution at the nonlinear resonance (●) with $A = 1$, displacement (a), velocity (b), contact force (c), x_2 DLFT-HBM (—), DLFT-HBM obstacle (▭), x_2 TI (▬).

Solutions of Eq. (46) are found by introducing a decaying exponential term $e^{-k\zeta t}$ for each k-th harmonic with ζ being a new unknown of the problem standing for the nonlinear modal damping, so that the solution is sought pseudo-periodic of the form

$$\mathbf{x}(t) \simeq \frac{\mathbf{a}_0}{2} + \sum_{k=1}^{N_\mathrm{h}} e^{-k\zeta t} \left(\mathbf{a}_k \cos(k\omega t) + \mathbf{b}_k \sin(k\omega t) \right). \tag{47}$$

In order to derive the harmonic balance equations with the displacement field Eq. (47), ζ is assumed to be small with respect to ω such that $\zeta \ll \omega$. This assumption means that the exponential decay is slow and thus negligible over one period, as supported by numerous papers in the literature [56, 70, 91]. The slow exponential decay hypothesis allows to neglect the exponential terms in the functions of the basis $t \mapsto e^{-k\zeta t} \cos(k\omega t)$ and $t \mapsto e^{-k\zeta t} \sin(k\omega t)$ in the Galerkin procedure. By doing so, the inner product, used to obtain the classical HBM

equation,

$$\langle f, g \rangle = \frac{2}{T} \int_0^T f(t) g(t) \mathrm{d}t \tag{48}$$

is still suitable for the complex nonlinear normal mode formalism. Using the new expression of the displacement field (47), the definition of the $\mathbf{Z}$ matrix is changed. The latter is still block diagonal where the blocks $\mathbf{Z}_k$ for $k > 0$ are modified by the presence of ζ and now read

$$\mathbf{Z}_k = \alpha \begin{bmatrix} \mathbf{K} - \dfrac{k\zeta}{\beta}\mathbf{C} - \dfrac{k^2\omega^2 - k^2\zeta^2}{\beta^2}\mathbf{M} & -\left(\dfrac{2k^2\omega\zeta}{\beta^2}\mathbf{M} - \dfrac{k\omega}{\beta}\mathbf{C}\right) \\ \left(\dfrac{2k^2\omega\zeta}{\beta^2}\mathbf{M} - \dfrac{k\omega}{\beta}\mathbf{C}\right) & \mathbf{K} - \dfrac{k\zeta}{\beta}\mathbf{C} - \dfrac{k^2\omega^2 - k^2\zeta^2}{\beta^2}\mathbf{M} \end{bmatrix} \quad \forall k \in [\![1, N_\mathrm{h}]\!]. \tag{49}$$

Even if the exponential terms are neglected in the inner product, these terms still induce supplementary ζ-dependent terms in the derivatives of $\mathbf{x}(t)$ that are accounted for in the new expression of $\mathbf{Z}$.

Since ζ is a new unknown of the problem, it is necessary to include a supplementary equation in order to close the equation system. For this purpose, a phase condition is retained. The phase condition consists in ensuring the value of displacement of a control dof, noted $\mathbf{x}_\mathrm{contr}$, to zero at the start of the period. This condition is written as the algebraic relation

$$\mathcal{P}_\zeta(\widetilde{\mathbf{x}}) = \mathbf{b}_\mathrm{contr} \cdot \left[\left(\mathbf{B}_{N_\mathrm{h}}(t_1) \right)^\top \widetilde{\mathbf{x}} \right] = \mathbf{x}_\mathrm{contr}(t_1) = 0 \tag{50}$$

where $\mathbf{B}_{N_\mathrm{h}}(t_1)$ is the Fourier basis evaluated at $t = t_1 = 0$ and $\mathbf{b}_\mathrm{contr}$ a boolean vector of size n. The latter is full of zeros but on the control dof number where it contains a one.

For continuation purposes, since the unknown vector is augmented of the parameter ζ, the arc-length parameterization equation is also modified such as

$$\mathcal{P}_\omega(\widetilde{\mathbf{x}}, \omega, \zeta) = \left\| \widetilde{\mathbf{x}} - \widetilde{\mathbf{x}}_{i-1} \right\|^2 + (\omega - \omega_{i-1})^2 + (\zeta - \zeta_{i-1})^2 - \mathrm{d}s^2 = 0 \tag{51}$$

where $\bullet_{i-1}$ refer to the different unknowns at the previous solution point and $\mathrm{d}s$ is the length of the step.

References

[1] A. H. Nayfeh and D. T. Mook. Nonlinear Oscillations. 1995. DOI: 10.1002/9783527617586.

[2] International Energy Agency. *Net Zero by 2050, a roadmap for the global energy sector*. 2021.

[3] Clean Aviation. *Clean sky 2*. https://www.clean-aviation.eu/clean-sky-2/programme-overview-and-structure. 2021.

[4] T. Detroux, L. Renson, L. Masset, and G. Kerschen. The harmonic balance method for bifurcation analysis of large-scale nonlinear mechanical systems. Comput. Methods Appl. Mech. Eng. Vol. 296 (2015), 18–38. DOI: 10.1016/j.cma.2015.07.017. oai : hal-03446374.

[5] L. Salles, B. Staples, N. Hoffmann, and C. Schwingshackl. Continuation techniques for analysis of whole aeroengine dynamics with imperfect bifurcations and isolated solutions. Nonlinear Dyn. Vol. 86, No. 3 (2016), 1897–1911. DOI: 10.1007/s11071-016-3003-y.

[6] T. Heinze, L. Panning-von Scheidt, and J. Wallaschek. Global detection of detached periodic solution branches of friction-damped mechanical systems. Nonlinear Dyn. Vol. 99, No. 3 (2020), 1841–1870. DOI: 10.1007/s11071-019-05425-4.

[7] L. Xie, S. Baguet, B. Prabel, and R. Dufour. Numerical Tracking of Limit Points for Direct Parametric Analysis in Nonlinear Rotordynamics. J. Vib. Acoust. Vol. 138, No. 2 (2016), 021007. DOI: 10.1115/1.4032182. oai : hal-01265919.

[8] N. Di Palma, B. Chouvion, and F. Thouverez. Parametric study on internal resonances for a simplified nonlinear blade model. Int. J. Non Linear Mech. Vol. 141 (2022), 103941. DOI: 10.1016/j.ijnonlinmec.2022.103941. oai : hal-03353678.

[9] C. M. Firrone and S. Zucca. Modelling Friction Contacts in Structural Dynamics and its Application to Turbine Bladed Disks. *Numerical Analysis*. 2011. Chap. 14. DOI: 10.5772/25128.

[10] J. Szwedowicz, R. Visser, W. Sextro, and P. A. Masserey. On Nonlinear Forced Vibration of Shrouded Turbine Blades. J. Turbomach. Vol. 130, No. 1 (2008), 011002. DOI: 10.1115/1.2218889.

[11] F. Massi, L. Baillet, O. Giannini, and A. Sestieri. Brake squeal: Linear and nonlinear numerical approaches. Mech. Syst. Sig. Process. Vol. 21, No. 6 (2007), 2374–2393. DOI: 10.1016/j.ymssp.2006.12.008.

[12] A. Millecamps, A. Batailly, M. Legrand, and F. Garcin. Snecma's Viewpoint on the Numerical and Experimental Simulation of Blade-Tip/Casing Unilateral Contacts. *Proceedings of the ASME Turbo Expo 2015*. 2015. DOI: 10.1115/GT2015-42682. oai : hal-01223582.

[13] T. Detroux, J.-P. Noël, L. N. Virgin, and G. Kerschen. Experimental study of isolas in nonlinear systems featuring modal interactions. PLoS One Vol. 13, No. 3 (2018), 25. DOI: 10.1371/journal.pone.0194452.

[14] E. P. Petrov. A Method for Parametric Analysis of Stability Boundaries for Nonlinear Periodic Vibrations of Structures With Contact Interfaces. J. Eng. Gas Turbines Power Vol. 141, No. 3 (2019), 031023. DOI: 10.1115/1.4040850.

[15] F. Mangussi and D. H. Zanette. Internal resonance in a vibrating beam: a zoo of nonlinear resonance peaks. PloS one Vol. 11, No. 9 (2016), e0162365. DOI: 10.1371/journal.pone.0162365. oai : hal-01463863.

[16] W. Koenigsberg and J. Dunn. Jump resonant frequency islands in nonlinear feedback control systems. IEEE T. Automat. Contr. Vol. 20, No. 2 (1975), 208–217. DOI: 10.1109/TAC.1975.1100914.

[17] A. Grolet and F. Thouverez. Computing multiple periodic solutions of nonlinear vibration problems using the harmonic balance method and Groebner bases. Mech. Syst. Sig. Process. Vol. 52-53 (2015), 529–547. DOI: 10.1016/j.ymssp.2014.07.015. oai : hal-02121532.

[18] M. Cenedese and G. Haller. How do conservative backbone curves perturb into forced responses? A Melnikov function analysis. Proc. R. Soc. A. Vol. 476, No. 2234 (2020), 20190494. DOI: 10.1098/rspa.2019.0494.

[19] S. Benacchio, C. Giraud-Audine, and O. Thomas. Effect of dry friction on a parametric nonlinear oscillator. Nonlinear Dyn. Vol. 108, No. 2 (2022), 1005–1026. DOI: 10.1007/s11071-022-07233-9. oai : hal-03754080.

[20] M. Volvert and G. Kerschen. Phase resonance nonlinear modes of mechanical systems. J. Sound Vib. Vol. 511 (2021), 116355. DOI: 10.1016/j.jsv.2021.116355.

[21] C.-H. Lamarque and A. T. Savadkoohi. Algebraic techniques and perturbation methods to approach frequency response curves. Int. J. Non Linear Mech. Vol. 144 (2022), 104096. DOI: 10.1016/j.ijnonlinmec.2022.104096. oai : hal-03749838.

[22] G. Gobat, L. Guillot, A. Frangi, B. Cochelin, and C. Touzé. Backbone curves, Neimark-Sacker boundaries and appearance of quasi-periodicity in nonlinear oscillators: application to 1:2 internal resonance and frequency combs in MEMS. Meccanica Vol. 56, No. 8 (2021), 1937–1969. DOI: 10.1007/s11012-021-01351-1. oai : hal-03242876.

[23] R. Alcorta, S. Baguet, B. Prabel, P. Piteau, and G. Jacquet-Richardet. Period doubling bifurcation analysis and isolated sub-harmonic resonances in an oscillator with asymmetric clearances. Nonlinear Dyn. Vol. 98, No. 4 (2019), 2939–2960. DOI: 10.1007/s11071-019-05245-6. oai : hal-02295420.

[24] R. Kuether, L. Renson, T. Detroux, C. Grappasonni, G. Kerschen, and M. Allen. Nonlinear normal modes, modal interactions and isolated resonance curves. J. Sound Vib. Vol. 351 (2015), 299–310. DOI: 10.1016/j.jsv.2015.04.035.

[25] T. Vadcard, Y. Colaïtis, A. Batailly, and F. Thouverez. Assessment of Two Harmonic Balance Method-Based Numerical Strategies for Blade-Tip/Casing Interactions: Application to Nasa Rotor67. J. Eng. Gas Turbines Power Vol. 144, No. 12 (2022). DOI: 10.1115/1.4055416. oai : hal-03775621.

[26] Y. Colaïtis. Stratégie numérique pour l'analyse qualitative des interactions aube/carter. PhD thesis. École Polytechnique Montréal, 2021. tel-03318777.

[27] A. Förster and M. Krack. An efficient method for approximating resonance curves of weakly-damped nonlinear mechanical systems. Comput. Struct. Vol. 169 (2016), 81–90. DOI: 10.1016/j.compstruc.2016.03.003.

[28] E. Sarrouy, A. Grolet, and F. Thouverez. Global and bifurcation analysis of a structure with cyclic symmetry. Int. J. Non Linear Mech. Vol. 46, No. 5 (2011), 727–737. DOI: 10.1016/j.ijnonlinmec.2011.02.005. oai : hal-00623630.

[29] N. J. Carpenter, R. L. Taylor, and M. G. Katona. Lagrange constraints for transient finite element surface contact. Int. J. Numer. Meth. Eng. Vol. 32, No. 1 (1991), 103–128. DOI: 10.1002/nme.1620320107. oai : hal-01389918.

[30] J. J. Moreau. Unilateral Contact and Dry Friction in Finite Freedom Dynamics. *Nonsmooth Mechanics and Applications*. 1988, pp. 1–82. DOI: 10.1007/978-3-7091-2624-0_1. oai : hal-01713847.

[31] M. Jean. The non-smooth contact dynamics method. Comput. Methods Appl. Mech. Eng. Vol. 177, No. 3-4 (1999), 235–257. DOI: 10.1016/S0045-7825(98)00383-1. oai : hal-01390459.

[32] L. Paoli and M. Schatzman. A Numerical Scheme for Impact Problems I: The One-Dimensional Case. SIAM J. Numer. Anal. Vol. 40, No. 2 (2002), 702–733. DOI: 10.1137/S0036142900378728. oai : hal-01885729.

[33] A. Batailly, M. Legrand, A. Millecamps, and F. Garcin. Numerical-Experimental Comparison in the Simulation of Rotor/Stator Interaction Through Blade-Tip/Abradable Coating Contact. J. Eng. Gas Turbines Power Vol. 134, No. 8 (2012), 082504. DOI: 10.1115/1.4006446. oai : hal-00746632.

[34] E. Piollet, F. Nyssen, and A. Batailly. Blade/casing rubbing interactions in aircraft engines: Numerical benchmark and design guidelines based on NASA rotor 37. J. Sound Vib. Vol. 460 (2019), 114878. DOI: 10.1016/j.jsv.2019.114878. oai : hal-02281666.

[35] A. Thorin, N. Guérin, M. Legrand, F. Thouverez, and P. Almeida. Nonsmooth Thermoelastic Simulations of Blade-Casing Contact Interactions. J. Eng. Gas Turbines Power Vol. 141, No. 2 (2019), 022502. DOI: 10.1115/1.4040857. oai : hal-01989188v1.

[36] E. Delhez, F. Nyssen, J.-C. Golinval, and A. Batailly. Assessment of Geometric Nonlinearities Influence On NASA Rotor 37 Response to Blade Tip/Casing Rubbing Events. J. Eng. Gas Turbines Power Vol. 143, No. 11 (2021). DOI: 10.1115/1.4051968. oai : hal-03343052.

[37] T. Vadcard, A. Batailly, and F. Thouverez. On Harmonic Balance Method-based Lagrangian contact formulations for vibro-impact problems. J. Sound Vib. Vol. 531 (2022), 116950. DOI: 10.1016/j.jsv.2022.116950. oai : hal-03665624.

[38] Y. Colaïtis and A. Batailly. The harmonic balance method with arc-length continuation in blade-tip/casing contact problems. J. Sound Vib. Vol. 502 (2021), 116070. DOI: 10.1016/j.jsv.2021.116070. oai : hal-03163560.

[39] Y. Colaïtis and A. Batailly. Stability analysis of periodic solutions computed for blade-tip/casing contact problems. J. Sound Vib. Vol. 538 (2022), 117219. DOI: 10.1016/j.jsv.2022.117219. oai : hal-03764770.

[40] Y. Colaïtis and A. Batailly. Stability Analysis of an Industrial Blade Accounting for a Blade-Tip/Casing Nonlinear Interface. J. Eng. Gas Turbines Power Vol. 145, No. 4 (2022), 041003. DOI: https://doi.org/10.1115/1.4055492. oai : hal-03778471.

[41] E. P. Petrov. Analysis of Bifurcations in Multiharmonic Analysis of Nonlinear Forced Vibrations of Gas Turbine Engine Structures With Friction and Gaps. J. Eng. Gas Turbines Power Vol. 138, No. 10 (2016), 12. DOI: 10.1115/1.4032906.

[42] P. Veerman and P. Holmes. The existence of arbitrarily many distinct periodic orbits in a two degree of freedom Hamiltonian system. Physica D Vol. 14, No. 2 (1985), 177–192. DOI: 10.1016/0167-2789(85)90177-0.

[43] P. Veerman and P. Holmes. Resonance bands in a two degree of freedom Hamiltonian system. Physica D Vol. 20, No. 2-3 (1986), 413–422. DOI: 10.1016/0167-2789(86)90043-6.

[44] K. Yagasaki. Periodic and homoclinic motions in forced, coupled oscillators. Nonlinear Dyn. Vol. 20, No. 4 (1999), 319–359. DOI: 10.1023/A:1008336402517.

[45] J. Shaw and S. W. Shaw. The onset of chaos in a two-degree-of-freedom impacting system. J. Appl. Mech. Vol. 56, No. 1 (1989), 168–174. DOI: 10.1115/1.3176040.

[46] S. W. Shaw and R. H. Rand. The transition to chaos in a simple mechanical system. Int. J. Non Linear Mech. Vol. 24, No. 1 (1989), 41–56. DOI: 10.1016/0020-7462(89)90010-3.

[47] M. Kunze and T. Küpper. Non-smooth dynamical systems: an overview. *Ergodic theory, analysis, and efficient simulation of dynamical systems*. Ed. by B. Fiedler. 2001, pp. 431–452. DOI: 10.1007/978-3-642-56589-2_19.

[48] T. L. Hill, S. A. Neild, and A. Cammarano. An analytical approach for detecting isolated periodic solution branches in weakly nonlinear structures. J. Sound Vib. Vol. 379 (2016), 150–165. DOI: 10.1016/j.jsv.2016.05.030.

[49] T. L. Hill, A. Cammarano, S. A. Neild, and D. J. Wagg. Interpreting the forced responses of a two-degree-of-freedom nonlinear oscillator using backbone curves. J. Sound Vib. Vol. 349 (2015), 276–288. DOI: 10.1016/j.jsv.2015.03.030.

[50] J. Yuan, Y. Sun, C. Schwingshackl, and L. Salles. Computation of damped nonlinear normal modes for large scale nonlinear systems in a self-adaptive modal subspace. Mech. Syst. Sig. Process. Vol. 162 (2022), 108082. DOI: 10.1016/j.ymssp.2021.108082.

[51] Y. Sun, A. Vizzaccaro, J. Yuan, and L. Salles. An extended energy balance method arfor resonance prediction in forced response of systems with non-conservative nonlinearities using damped nonlinear normal mode. Nonlinear Dyn. Vol. 103 (2021), 3315–3333. DOI: 10.1007/s11071-020-05793-2.

[52] Y. A. Kuznetsov. Elements of applied bifurcation theory. 1998. DOI: 10.1007/978-1-4757-3978-7.

[53] P. Wriggers. Computational contact mechanics. 2nd ed. 2006.

[54] M. Krack and J. Gross. Harmonic Balance for Nonlinear Vibration Problems. 2019. DOI: 10.1007/978-3-030-14023-6.

[55] T. M. Cameron and J. H. Griffin. An Alternating Frequency/Time Domain Method for Calculating the Steady-State Response of Nonlinear Dynamic Systems. J. Appl. Mech. Vol. 56, No. 1 (1989), 149–154. DOI: 10.1115/1.3176036. oai : hal-01333697.

[56] M. Krack, L. P. von Scheidt, and J. Wallaschek. A method for nonlinear modal analysis and synthesis: Application to harmonically forced and self-excited mechanical systems. J. Sound Vib. Vol. 332, No. 25 (2013), 6798–6814. DOI: 10.1016/j.jsv.2013.08.009.

[57] S. Karkar, B. Cochelin, and C. Vergez. A high-order, purely frequency based harmonic balance formulation for continuation of periodic solutions: The case of non-polynomial nonlinearities. J. Sound Vib. Vol. 332, No. 4 (2013), 968–977. DOI: 10.1016/j.jsv.2012.09.033. oai : hal-00758184.

[58] L. Peletan, S. Baguet, M. Torkhani, and G. Jacquet-Richardet. Quasi-periodic harmonic balance method for rubbing self-induced vibrations in rotor–stator dynamics. Nonlinear Dyn. Vol. 78, No. 4 (2014), 2501–2515. DOI: 10.1007/s11071-014-1606-8. oai : hal-01061265.

[59] W.-J. Kim and N. Perkins. Harmonic balance/Galerkin method for non-smooth dynamic systems. J. Sound Vib. Vol. 261, No. 2 (2003), 213–224. DOI: 10.1016/S0022-460X(02)00949-5. oai : hal-01693093.

[60] N. Coudeyras, S. Nacivet, and J.-J. Sinou. Periodic and quasi-periodic solutions for multi-instabilities involved in brake squeal. J. Sound Vib. Vol. 328, No. 4-5 (2009), 520–540. DOI: 10.1016/j.jsv.2009.08.017. oai : hal-00425156.

[61] C. Duan, T. E. Rook, and R. Singh. Sub-harmonic resonance in a nearly pre-loaded mechanical oscillator. Nonlinear Dyn. Vol. 50, No. 3 (2007), 639–650. DOI: 10.1007/s11071-006-9185-y.

[62] F. Fontanela, A. Vizzaccaro, J. Auvray, B. Niedergesäß, A. Grolet, L. Salles, and N. Hoffmann. Nonlinear vibration localisation in a symmetric system of two coupled beams. Nonlinear Dyn. Vol. 103, No. 4 (2021), 3417–3428. DOI: 10.1007/s11071-020-05760-x.

[63] S. Nacivet, C. Pierre, F. Thouverez, and L. Jezequel. A dynamic Lagrangian frequency–time method for the vibration of dry-friction-damped systems. J. Sound Vib. Vol. 265, No. 1 (2003), 201–219. DOI: 10.1016/S0022-460X(02)01447-5. oai : hal-01635272.

[64] S. Quaegebeur, B. Chouvion, and F. Thouverez. Nonlinear dynamic analysis of three-dimensional bladed-disks with frictional contact interfaces based on cyclic reduction strategies. Int. J. Solids Struct. Vol. 236-237 (2022), 111277. DOI: 10.1016/j.ijsolstr.2021.111277.

[65] R. M. Rosenberg. Normal Modes of Nonlinear Dual-Mode Systems. J. Appl. Mech. Vol. 27, No. 2 (1960), 263–268. DOI: 10.1115/1.3643948.

[66] S. Shaw and C. Pierre. Non-linear normal modes and invariant manifolds. J. Sound Vib. Vol. 150, No. 1 (1991), 170–173. DOI: 10.1016/0022-460X(91)90412-D. oai : hal-01310674.

[67] F. Georgiades, M. Peeters, G. Kerschen, J. C. Golinval, and M. Ruzzene. Modal Analysis of a Nonlinear Periodic Structure with Cyclic Symmetry. AIAA J. Vol. 47, No. 4 (2009), 1014–1025. DOI: 10.2514/1.40461. oai : hal-01385735.

[68] M. Peeters, R. Viguié, G. Sérandour, G. Kerschen, and J.-C. Golinval. Nonlinear normal modes, Part II: Toward a practical computation using numerical continuation techniques. Mech. Syst. Sig. Process. Vol. 23, No. 1 (2009), 195–216. DOI: 10.1016/j.ymssp.2008.04.003.

[69] L. Renson, G. Kerschen, and B. Cochelin. Numerical computation of nonlinear normal modes in mechanical engineering. J. Sound Vib. Vol. 364 (2016), 177–206. DOI: 10.1016/j.jsv.2015.09.033.

[70] D. Laxalde and F. Thouverez. Complex non-linear modal analysis for mechanical systems: Application to turbomachinery bladings with friction interfaces. J. Sound Vib. Vol. 322, No. 4-5 (2009), 1009–1025. DOI: 10.1016/j.jsv.2008.11.044. oai : hal-00343494v3.

[71] A. Grolet and F. Thouverez. Free and forced vibration analysis of a nonlinear system with cyclic symmetry: Application to a simplified model. J. Sound Vib. Vol. 331, No. 12 (2012), 2911–2928. DOI: 10.1016/j.jsv.2012.02.008.

[72] G. Von Groll and D. Ewins. The harmonic balance method with arc-length continuation in rotor/stator contact problems. J. Sound Vib. Vol. 241, No. 2 (2001), 223–233. DOI: 10.1006/jsvi.2000.3298. oai : hal-01333704.

[73] M. Krack. Nonlinear modal analysis of nonconservative systems: Extension of the periodic motion concept. Comput. Struct. Vol. 154 (2015), 59–71. DOI: 10.1016/j.compstruc.2015.03.008.

[74] Y. Sun, J. Yuan, A. Vizzaccaro, and L. Salles. Comparison of different methodologies for the computation of damped nonlinear normal modes and resonance prediction of systems with non-conservative nonlinearities. Nonlinear Dyn. Vol. 104, No. 4 (2021), 3077–3107. DOI: 10.1007/s11071-021-06567-0.

[75] A. Thorin, P. Delezoide, and M. Legrand. Nonsmooth Modal Analysis of Piecewise-Linear Impact Oscillators. SIAM J. Appl. Dyn. Syst. Vol. 16, No. 3 (2017), 1710–1747. DOI: 10.1137/16M1081506. oai : hal-01298983v2.

[76] D. Pun, S. Lau, S. Law, and D. Cao. FORCED VIBRATION ANALYSIS OF A MULTIDEGREE IMPACT VIBRATOR. J. Sound Vib. Vol. 213, No. 3 (1998), 447–466. DOI: https://doi.org/10.1006/jsvi.1997.1494.

[77] S. F. Masri. Steady-State Response of a Multidegree System With an Impact Damper. J. Appl. Mech. Vol. 40, No. 1 (1973), 127–132. DOI: 10.1115/1.3422910.

[78] D. J. Wagg. Multiple non-smooth events in multi-degree-of-freedom vibro-impact systems. Nonlinear Dyn. Vol. 43 (2006), 137–148.

[79] M. Attar, A. Karrech, and K. Regenauer-Lieb. Non-linear modal analysis of structural components subjected to unilateral constraints. J. Sound Vib. Vol. 389 (2017), 380–410. DOI: https://doi.org/10.1016/j.jsv.2016.11.012.

[80] S. Shaw and P. Holmes. A periodically forced piecewise linear oscillator. J. Sound Vib. Vol. 90, No. 1 (1983), 129–155. DOI: https://doi.org/10.1016/0022-460X(83)90407-8.

[81] V. Acary and B. Brogliato. Numerical methods for nonsmooth dynamical systems: applications in mechanics and electronics. L. N. App. C. M. 35. 2008. DOI: 10.1007/978-3-540-75392-6.

[82] R. Seydel. Practical Bifurcation and Stability Analysis. 2010. DOI: 10.1007/978-1-4419-1740-9.

[83] M. Cenedese and G. Haller. Stability of forced–damped response in mechanical systems from a Melnikov analysis. Chaos: An Interdisciplinary Journal of Nonlinear Science Vol. 30, No. 8 (2020).

[84] L. Reid and R. D. Moore. *Design and overall performance of four highly loaded, high speed inlet stages for an advanced high-pressure-ratio core compressor*. rapport technique. https://ntrs.nasa.gov/citations/19780025165. NASA Lewis Research Center Cleveland, OH, USA, 1978.

[85] E. Benini and R. Biollo. Aerodynamics of swept and leaned transonic compressor-rotors. Appl. Energ. Vol. 84, No. 10 (2007), 1012–1027. DOI: doi:10.1016/j.apenergy.2007.03.003.

[86] A. Ameri. NASA rotor 37 CFD code validation. *47th AIAA Aerospace Sciences Meeting including The New Horizons Forum and Aerospace Exposition*. 2009. DOI: 10.2514/6.2009-1060.

[87] J. D. Denton. Lessons from rotor 37. J. Therm. Sci. Vol. 6, No. 1 (1997), 1–13. DOI: 10.1007/s11630-997-0010-9.

[88] W. Cui, X. Xiang, Q. Zhao, and J. Xu. The effect of sweep on flowfields of a highly loaded transonic rotor. Aerosp. Sci. Technol. Vol. 58 (2016), 71–81. DOI: 10.1016/j.ast.2016.08.002.

[89] D. Huebler. *Rotor 37 and stator 37 assembly. Records of the National Aeronautics and Space Administration, 1903 - 2006. Photographs relating to agency activities, facilities and personnel, 1973 - 2013*. https://catalog.archives.gov/id/17468389. 1977.

[90] R. R. Craig and M. C. C. Bampton. Coupling of substructures for dynamic analyses. AIAA J. Vol. 6, No. 7 (1968), 1313–1319. DOI: 10.2514/3.4741. oai : hal-01537654.

[91] C. Joannin, B. Chouvion, F. Thouverez, J.-P. Ousty, and M. Mbaye. A nonlinear component mode synthesis method for the computation of steady-state vibrations in non-conservative systems. Mech. Syst. Sig. Process. Vol. 83 (2017), 75–92. DOI: 10.1016/j.ymssp.2016.05.044.